

---

Electronic Thesis and Dissertation Repository

---

9-28-2023 11:00 AM

# Optimizing and Evaluating Zinc Oxide Nanoparticles as a Matrix for Matrix-Assited Laser/ Desorption Ionization Mass Spectrometry for Small Molecule Detection in Rodent Brain Tissue

Juan Pablo Galindo, *Western University*

Supervisor: Yeung, Ken, *The University of Western Ontario*

A thesis submitted in partial fulfillment of the requirements for the Master of Science degree in Chemistry

© Juan Pablo Galindo 2023

Follow this and additional works at: <https://ir.lib.uwo.ca/etd>

 Part of the [Analytical Chemistry Commons](#)

---

## Recommended Citation

Galindo, Juan Pablo, "Optimizing and Evaluating Zinc Oxide Nanoparticles as a Matrix for Matrix-Assited Laser/ Desorption Ionization Mass Spectrometry for Small Molecule Detection in Rodent Brain Tissue" (2023). *Electronic Thesis and Dissertation Repository*. 9712.  
<https://ir.lib.uwo.ca/etd/9712>

This Dissertation/Thesis is brought to you for free and open access by Scholarship@Western. It has been accepted for inclusion in Electronic Thesis and Dissertation Repository by an authorized administrator of Scholarship@Western. For more information, please contact [wlsadmin@uwo.ca](mailto:wlsadmin@uwo.ca).

## **Abstract**

Matrix-assisted laser/desorption ionization (MALDI) is the preferred method for mass spectrometry imaging (MSI) due to its high spatial resolution. Detecting small molecules like  $\gamma$ -aminobutyric acid (GABA) and glutamate, which are the main inhibitory and excitatory neurotransmitters respectively, proves challenging as their low masses conflict with background signals from most matrices.

This work optimizes zinc oxide nanoparticles (ZnO NP) as a matrix, focusing on GABA and Glutamate detection. Its absence of background signals makes ZnO suitable for small molecule detection. Its shortcomings, especially batch-to-batch variability, were mitigated through filtration and sonication before deposition, achieving high-resolution imaging of rat brain tissue sections.

To assess ZnO NP viability, MALDI MSI was employed to relatively quantify glutamate, glutamine, and GABA in brain tissue sections from adolescent rat brains exposed to  $\Delta$ -9-tetrahydrocannabinol ( $\Delta$ -9-THC) through edibles in the nucleus accumbens (NAc) subregions. ZnO NP consistently detected all, revealing a downregulation in each molecule in both subregions.

## **Keywords**

Mass Spectrometry imaging, MALDI, ZnO nanoparticles, matrix optimization, small molecules, neurotransmitters, rat brains, THC edibles, adolescent chronic exposure, relative quantitation.

## Summary for Lay Audience

Scientists use a technique called Mass spectrometry Imaging (MSI) to study and analyze the composition and location of different chemicals in biological tissue in a fast and practical manner. They commonly used a method called Matrix-assisted laser desorption/ionization (MALDI), where a specific substance, denominated matrix, is used to detect the target chemicals within the sample. MALDI MSI creates molecular images for many chemical compounds, depending on the matrix employed.

One promising material for MALDI is Zinc oxide nanoparticles (ZnO NP). It can detect a variety of small molecules and neurotransmitters. ZnO NP can detect crucial neurotransmitters such as  $\gamma$ -aminobutyric acid (GABA) and glutamate in mouse and rat brain tissues. However, the ZnO NP samples that are available in commercial stores, are known to exhibit variations in size and quality across different batches and commercial providers. As a result, an optimization protocol was developed to minimize these variables, ensuring that the matrix consistently produces high-quality results.

The optimized ZnO NP matrix was used in a comprehensive long-term study involving chronic  $\Delta$ -9-tetrahydrocannabinol (THC) edible administration to adolescent rats using Nutella as the THC vehicle. Constant exposure to THC, particularly during adolescence, has been shown to alter the total levels of GABA, Glutamate, and Glutamine in the prefrontal cortex brain region. These neurochemical damages are reported to persist into adulthood. The MALDI studies reveal a decrease in total GABA, glutamine, and glutamate levels in the various subregions of adolescent rat brains.

## **Co-Authorship Statement**

All data presented in this thesis was collected by the author. This thesis was edited by Dr. Ken Yeung. Animal care and THC administration was done by Dr. De Vuono from the Dr. Laviolette Lab.

## **Acknowledgments**

First, I would like to express my sincere gratitude to my supervisor, Dr. Ken Yeung, for his invaluable advice, unwavering support, and vast patience throughout the past couple of years. His guidance not only shaped my research endeavors but also fostered an environment of respect and encouragement in the lab. His insights, keen observations, and innovative ideas significantly contributed to my growth as a researcher and scientist. This work would not have been possible without his consistent and dedicated mentorship, making him an indispensable part of my academic journey.

I extend my heartfelt appreciation to Dr. Steven R. Laviolette, our principal research collaborator, for his thought-provoking ideas that presented themselves as challenging and exciting neuroscience projects.

I am deeply indebted to Western University and Dr. Ken Yeung for their generous financial support, which played a crucial role in enabling the successful completion of this thesis. The state-of-the-art facilities and laboratory equipment provided by Western University were instrumental in the development and execution of my research.

I am immensely grateful to my esteemed committee members, Dr. Lars Konerman and Dr. Mark Sumarah, whose constructive comments and feedback were of paramount importance in shaping the trajectory of my work. Their time and expertise are greatly appreciated, and their contributions will not be forgotten. I also extend this gratitude to the entirety of my examination panel.

A special acknowledgement goes to Dr. De Vuono, for her invaluable contributions to the animal work for the adolescent THC project. I am particularly thankful for her patience, especially during the region selection process. Her insights into the biological field also helped me gain a better understanding of the project's scope, fueling my passion for THC research.

I am deeply appreciative of the vibrant and supportive community within the Yeung Lab, represented by Mathusha Pusparajah and Samantha Cousineau. Their warm welcome and continuous encouragement fostered an environment where I felt both valued and respected. I also owe my gratitude to Mohammed Halit Sarikahya, whose contagious passion for neuroscience served as a motivating force in our collaborative efforts. A special mention is reserved for Samantha Cousineau, whose mentorship over the past two years felt like a second supervisor on many occasions. Her guidance and the discussions we shared greatly contributed to many of the advancements in my research, and she was someone I learned a lot from. Similar sentiments extend to Kristina Jurcic, whose mentorship, especially in the initial stages of my research, was pivotal in mastering various techniques, including the operation of our mass spectrometer. Her patient guidance, knowledge, and unwavering support were integral to the success of my work.

I feel deeply grateful for the many friends I made in London. I am particularly thankful to Dean Barlett, Margarita Medrana, Mary Helen Youseph, Alejandro Garcia, Julieta Navarrete, Alexander Escobar, and Ali Ruiz for the emotional support and encouragement they gave me through this journey.

Lastly, I would express my profound love and gratitude to my family, especially my parents Álvaro Galindo and María Fernanda Lazo, and my brother, Daniel Galindo Lazo. Despite the physical distance of over 3000 km, their unwavering support and love have been the foundational pieces of my achievements. Without them, none of my achievements would have been possible.

# Table of Contents

<b>Abstract</b> .....	<b>ii</b>
<b>Co-Authorship Statement</b> .....	<b>iv</b>
<b>Table of Contents</b> .....	<b>vii</b>
<b>List of Figures</b> .....	<b>x</b>
<b>List of Equations</b> .....	<b>xii</b>
<b>List of Abbreviations</b> .....	<b>xiii</b>
<b>Chapter 1: Introduction of Small Molecule Detection and Imaging by Mass Spectrometry</b> .....	<b>1</b>
1.1 Mass Spectrometry for the Detection of Small Molecules .....	2
1.1.2 Principles of Mass Spectrometry Imaging .....	4
1.2 Ionization Techniques in Mass Spectrometry Imaging.....	5
1.2.1 Liquid Extraction Surface Analysis .....	5
1.2.2 Secondary Ion Mass Spectrometry .....	6
1.2.3 Desorption electrospray ionization mass spectrometry .....	8
1.2.4 Matrix-Assisted Laser/ Desorption Ionization .....	9
1.3 MALDI MSI for Small Molecules .....	12
1.3.1 Biological Tissue Preparation for MALDI .....	12
1.3.2 Brief Overview of the Matrix in MALDI MSI .....	14
1.3.3 Matrix Deposition .....	15
1.4 Mass Analyzers for MSI .....	18
1.4.1 Mass Accuracy and its Meaning for MALDI MSI .....	18
1.4.2 Time-of-Flight (TOF) Analyzer.....	19
1.4.3 Fourier-Transform Ion Cyclotron Resonance Analyzer .....	20
1.4.4 Orbitrap Analyzer .....	21
1.4.5 MS Detector .....	22
1.5 Matrices in MALDI for Small Molecule Detection .....	23
1.5.1 Matrix Selection for Small Molecules .....	23
1.5.2 Ionization Methods Among Different Matrices.....	24
1.5.3 Reactive Matrices for Small Molecule Detection .....	25
1.5.4 Organic Matrices for Small Molecule Detection .....	28
1.5.5 Metals and Metal Oxide Nanoparticles for Small Molecule Detection .....	29
1.6 Conclusion .....	31

1.7	References .....	32
<b>Chapter 2. Optimization of ZnO Nanoparticles for the Detection and Imaging of Small Molecules in Rodent Brain Tissue Using Matrix-Assisted Laser/Desorption Ionization Mass Spectrometry .....</b>		
2.1	Introduction .....	38
2.2	Methodology and Materials .....	40
2.2.1	Chemicals and Supplies .....	40
2.2.2	Matrix Solution Filtering and Preparation .....	40
2.2.3	DLS Size Determination of Filtered Nanoparticle Dispersions .....	41
2.2.4	UV-Vis Concentration Determination of Filtered Nanoparticle Dispersions ..	41
2.2.5	Rodent Tissue Sectioning and Preparation .....	42
2.2.6	Matrix Deposition .....	42
2.2.7	MALDI MS Analysis and Data Processing .....	42
2.3	Results and Discussion.....	43
2.3.1	DLS Analysis of Particle Size Before and After Filtration of the ZnO NP Dispersion .....	43
2.3.2	Concentration Analysis of Filtered ZnO Dispersion.....	44
2.3.3	Optimization of Matrix Deposition on Rodent Brain Tissue for Small Molecule Detection .....	47
2.3.3.1	ZnO Nanoparticle Spotting on Standards Analysis .....	47
2.3.3.2	Matrix Deposition Parameters Optimization .....	48
2.4	Comparison Between Optimized ZnO NP and Other Matrices for the Detection of Small Molecules.....	50
2.5	Conclusion .....	53
2.6	References.....	54
<b>Chapter 3. Relative Quantitation of Neurotransmitters and Other Small Molecules in Brains from Adolescent Rats Subjected to Edible Delta-9-Tetrahydrocannabinol (THC) Consumption Using Optimized ZnO Nanoparticles by Matrix-Assisted Laser/Desorption Ionization Mass Spectrometry. ....</b>		
3.1	Introduction .....	56
3.2	Experimental Section .....	58
3.2.1	Chemicals and Supplies .....	58
3.2.2	Animals and Housing.....	58
3.2.3	Drug Administration .....	58
3.2.4	Sample Preparation for MSI .....	59
3.2.5	MALDI MS Data Processing and Analysis .....	60



3.3 Results and Discussion.....	61
3.3.1 Identification of Small Molecules GABA, Glutamate, and Glutamine in the Rodent Brain Sections.....	61
3.3.2 Relative Quantitation of Small Molecules Glutamate, GABA, and Glutamine between sexes and THC-treated and Vehicle-treated Rat Brains. ....	62
3.3.3 Comparison Between the Relative Quantitation of the Matrices ZnO Nanoparticles and FMP-10 for GABA detection in THC-treated and Vehicle-treated Rat Brains.....	67
3.4 Comparison with Literature .....	70
3.5 Conclusion .....	72
3.6 References.....	73
<b>Chapter 4. Conclusions and Future Work.....</b>	<b>74</b>
4.1 Conclusions and Future Work.....	75
4.2 References.....	78
<b>Curriculum Vitae .....</b>	<b>79</b>

## List of Figures

<b>Figure 1.1</b> Diagram of the SIMS process [15] .....	7
<b>Figure 1.2.</b> Schematic of operation of a normal DESI experiment [21] .....	8
<b>Figure 1.3.</b> MALDI ionization process .....	10
<b>Figure 1.4.</b> MALDI MSI scheme [3] .....	12
<b>Figure 1.5.</b> The cryo-sectioning of a mouse brain. The anti-roll bar prevents the cut sections from curling up (left). The section is thaw-mounted to an ITO glass slide and is stored at -80 °C until used [34].....	13
<b>Figure 1.6.</b> A) A traditional linear TOF path where $A_2$ and $A_1$ are ions with different masses and kinetic energies. B) A reflectron TOF path where $A_2$ and $A_1$ are ions with different masses and kinetic energies [45].....	20
<b>Figure 1.7.</b> Schematic diagram of FT-ICR mass analyzer (left) and the actual picture of the cylindrical cell of one (right) [47].....	21
<b>Figure 1.8.</b> Diagram of a typical Orbitrap mass analyzer [48].....	22
<b>Figure 1.9.</b> Reaction mechanism of a) TAHS, b) CA, and c) DPP-TFB [61].....	27
<b>Figure 1.10.</b> Schematic of the reaction between the FMP-10 matrix and phenolic hydroxyls and amines [65].....	28
<b>Figure 2.1.</b> DLS size distribution before filtration (red) and after filtration (blue) for the batch bought in September 2022 .....	44
<b>Figure 2.2.</b> ZnO NP dispersion before (left) and after (right) sonication. The heterogeneous concentration before sonicating can be explained by the bigger nanoparticles sinking to the bottom. ....	45
<b>Figure 2.3.</b> Reproducibility of concentration after filtration of the ZnO NP dispersion .....	46
<b>Figure 2.4.</b> Concentration of ZnO NP dispersion dropped over time due to the gradual settling of NP .....	46
<b>Figure 2.5.</b> Positive ion mass spectrum of a 0.2 mg/mL GABA standard: 103.984 $m/z$ $[M + H]^+$ ; 126.091 $m/z$ , $[M + Na]^+$ ; 142.009 $m/z$ , $[M + K]^+$ ; 148.137 $m/z$ , $[M + 2Na - H]^+$ ; $m/z$ 164.013 $m/z$ $[M - H + Na + K]^+$ ; 180.003 $m/z$ $[M - H + 2K]^+$ with 5 mg/mL filtered ZnO matrix solution. ....	47
<b>Figure 2.6.</b> The peak intensities of (A) GABA and (B) glutamate determined from the nucleus accumbens core region of rat brain tissue after different numbers of NP spraying passes.....	49
<b>Figure 2.7.</b> MSI spatial distribution in positive mode.....	49
of GABA (left), Glutamate (center), and Cholesterol (right) at Bregma -6.00 mm and Bregma 2.52 mm, respectively at 20 passes with a raster size of 70 $\mu\text{m}$ . ....	49

**Figure 2.8.** GABA molecule detected with ZnO NP as a matrix (left) and FMP-10 (right). The FMP-10 signal is higher but has less defined spatial features. .... 51

**Figure 2.9.** Average mass spectra in positive ion mode of the nucleus accumbens core region of the rat brain for FMP-10 (top). Average mass spectrum in positive ion mode of the nucleus accumbens core region of a rat brain for ZnO NP (button)..... 52

**Figure 3.1.** Schematic diagrams showing ROIs ..... 62

**Figure 3.2.** Peak area ratios of GABA between THC-treated and vehicle-treated adolescent rat brains in the NAc core (left) and shell (right) regions. Asterisks indicate that the featured ratio is statistically significant in the one sample T-test (\*\*p < 0.01) ..... 63

**Figure 3.3.** Peak area ratios of Glutamate between THC-treated and vehicle-treated adolescent rat brains in the NAc core (left) and shell (right) regions. Asterisks indicate that the featured ratio is statistically significant in the one sample T-test (\*\*p < 0.01) ..... 64

**Figure 3.4.** Peak area ratios of Glutamine between THC-treated and vehicle-treated adolescent rat brains in the NAc core (left) and shell (right) regions. Asterisks indicate that the featured ratio is statistically significant in the one sample T-test (\*\*p < 0.01) ..... 65

**Figure 3.5.** Diagram of the Glutamate- Glutamine cycle and the GABA- Glutamate cycle. Alongside the diagram, ion images of all three analytes obtained by ZnO NP are shown. .... 66

**Figure 3.6.** Peak area ratios of GABA between THC-treated and vehicle-treated adolescent rat brains in the NAc core (left) and shell (right) regions using FMP-10. Asterisks indicate that the featured ratio is statistically significant in the one-sample T-test (\* p < 0.01) ..... 68

## List of Equations

		Page
$R = \frac{m/z}{\Delta(m/z)}$	Eq. 1.1	18
$Mass\ Accuracy = \frac{Measured\ Mass - True\ Mass}{True\ Mass} \times 1,000,000$	Eq. 1.2	19

## List of Abbreviations

$\alpha$	alpha
$\gamma$	gamma
$\Delta$	delta
$\Delta$ -9-THC	$\Delta$ -9-tetrahydrocannabinol
$\Delta(m/z)$	width of the peak at 50% of its peak height
$\mu$ L	microliter (1 mL= $10^{-6}$ L)
$\mu$ LESA	Micro Liquid Extraction Surface Analysis
$\mu$ m	micrometers (1 mg= $10^{-6}$ g)
$^{\circ}$ C	centigrade
ACN	acetonitrile
AgLDI	silver-assisted laser desorption ionization
Au-S	gold-sulfur bonds
CA	4-hydroxy-3-methoxycinnamaldehyde
CB1Rs	cannabinoid type 1 receptors
CD	chemical derivatization
CE	capillary electrophoresis
CHCA	$\alpha$ -cyano-4-hydroxycinnamic acid
D <sub>4</sub> -CHCA	deuterated $\alpha$ -cyano-4-hydroxycinnamic acid
Da	dalton
DAN	1,5-diaminophthalene
DESI	desorption electrospray ionization mass spectrometry
DHB	2,5-dihydroxybenzoic acid
DLS	Dynamic Light Scattering
DMCA	3,4-Dimethoxycinnamic Acid
DPP-TFB	2,3-diphenyl-pyranylium tetrafluoro-borate
ESI	electrospray ionization
FAIMS	High Field Asymmetric Waveform Ion Mobility Spectrometry

FMP-10	4-(anthracen-9-yl)-2-fluoro-1-methylpyridin-1-ium iodide
FT-IRC	Fourier-transform ion cyclotron resonance
g	gram
GABA	$\gamma$ -aminobutyric acid
GC	gas chromatography
IM	ion mobility
ITO	indium tin oxide
K <sup>+</sup>	potassium ion
kDa	kilodalton
kg	kilogram
LC	liquid chromatography
LESA	liquid extraction surface analysis
m	mass of the ion
M <sup>+</sup>	molecular ion
<i>m/z</i>	mass-to-charge-ratio
MALDI	matrix-assisted laser desorption ionization
min	minute
mg	milligram (1 mg= 10 <sup>-3</sup> g)
mL	milliliter (1 mL= 10 <sup>-3</sup> L)
mm	millimetre (1 mm= 10 <sup>-3</sup> m)
MS	mass spectrometry
MS/MS	tandem mass spectrometry
MSI	mass spectrometry imaging
Na <sup>+</sup>	sodium ion
NAc	nucleus accumbens
ng	nanogram (1 ng= 10 <sup>-9</sup> g)
nm	nanometres (1 nm= 10 <sup>-9</sup> m)
NP	nanoparticles
NTs	neurotransmitters
OTC	on-tissue chemical derivatization
p	p-values in the Student's T-test

PDI	polydispersity index
PFC	prefrontal cortex
PND	postnatal day
ppm	parts per million
psi	pounds per square inch
R	resolution
R <sup>2</sup>	square of the correlation coefficient
ROI	region of interest
RSD	relative standard deviation
SD	standard deviation
SEM	standard of error of the mean
SIMS	secondary ion mass spectrometry
TAHS	p-N, N, N-trimethylammonioanilyl N-hydroxysuccinimidyl
carbamate iodide	
TFA	trifluoroacetic acid
TIC	total ion count
TOF	time-of-flight
UV	ultraviolet
VEH	vehicle
vol	volume
wt	weight
ZnO NP	zinc oxide nanoparticles

# **Chapter 1: Introduction of Small Molecule Detection and Imaging by Mass Spectrometry**



## 1.1 Mass Spectrometry for the Detection of Small Molecules

In chemical biology, small molecules are chemical compounds with a molecular weight of less than a kilodalton (kDa). Molecules that fit this distinction include certain lipids, drugs, amino acids, peptides, fatty acids, organic acids, and neurotransmitters, among many others [1]. Small molecules are common in the body, especially in the brain. Many of these metabolites play important roles in key neurological processes that enable the brain to properly function. The best examples of small molecules playing a crucial part in brain function are neurotransmitters. Neurotransmitters are known as the “chemical messengers” of the brain. As such, they are tasked with sending information between neurons and a target cell, which can be a muscle cell, gland, or another neuron. Neurotransmitters can either excite or inhibit signals in the brain, leading to changes in chemical and physical responses in the body [2]. Consequently, they are critical for many of the functions in various biological systems. Naturally, the accurate detection of neurotransmitters and other small molecules in the brain can be key to developing an early and appropriate diagnosis.

One way to properly assess the abundance of small molecules in the brain is by employing Mass Spectrometry (MS). In this technique, the molecular ions and/or their fragments are separated by the mass-to-charge ratio, known as  $m/z$ , giving both qualitative and quantitative data for each ion [3].

### 1.1.1 Principles of Mass Spectrometry

Mass Spectrometry (MS) is a powerful analytical tool to identify and quantify chemical compounds, providing information regarding their structure and composition. An MS process begins with the ionization of the sample, followed by an acceleration and deflection of the ionized molecules. In this step, the molecules are subjected to a strong electrical field where each ion moves at a specific speed based on their mass and charge. The ions are then deflected by a magnetic field separating according to their  $m/z$ . Finally, the separated ions enter a mass analyzer, which

measures their  $m/z$  and generates a graph showing ion signals in peaks at different  $m/z$  values; this graph is known as a mass spectrum [4].

As mentioned before, MS measures the  $m/z$  abundances of gas-phase ions to detect and quantify a specific set of molecules from a sample. The identification of a molecule comes from its mass accuracy and characteristic molecular fragments. MS has high sensitivity, good resolution, good mass accuracy, and a wide dynamic range [5]. MS also allows for direct coupling with chemical separation apparatuses, making it a potent combination for specifically targeted analysis in biological samples. Examples of these separating techniques are ion mobility (IM), capillary electrophoresis (CE), gas chromatography (GC), and liquid chromatography (LC). The last two are the most popular ones for their separating capabilities, high reproducibility, and resistance to impurities, known as GC-MS and LC-MS respectively [6].

GC utilizes a gaseous mobile phase, usually an inert gas like Helium, to carry the sample through a chromatographic column. GC-MS is generally used for more volatile compounds, as it is well-suited for the separation of organic, volatile compounds such as alcohols and ethers. On the other hand, LC-MS is the most popular analytical technique in small molecule analysis thanks to its wide molecular coverage and practicality. It utilizes a liquid mobile phase to carry the sample through a column, and the sample in liquid form and separate the sample based on its polarity. LC is generally coupled with an electrospray ionization (ESI) MS source to facilitate the detection of different small molecules. As can be seen, mass spectrometry is an exciting field that continues to advance. Numerous new developments are being made with mass detectors, mass analyzers, data analysis methods, and many other tools that allow scientists to explore small molecules.

### 1.1.2 Principles of Mass Spectrometry Imaging

Mass Spectrometry Imaging (MSI) is an imaging technique where mass spectra are systematically acquired from every point of a sample by scanning and ionizing at the same time over the sample. MSI takes advantage of the selectivity and sensitivity of mass spectrometry, and it does not rely on any labeling of compounds [7]. An MSI experiment takes one or several hours depending on the size of the sample and the raster size used for the scanning/ ionization. After the MSI run is done, a collection of thousands of mass spectra yields an image where each pixel is a mass spectrum. Each extracted ion will give a different image which helps in assessing the molecular distribution of each target analyte in the sample. These images are usually shown on a heat map where the color represents signal intensity. The higher the intensity the brighter the color will be. One of the biggest assets of MSI is its non-targeted nature meaning that any sample can be studied without a deep knowledge about it. As a result, one can simply browse through the ion masses to check for any changes or to retrospectively analyze and test new hypotheses.

As with other mass spectrometry techniques, the ionization step determines the analytes detected in the sample. However, in MSI, the ionization technique also determines the spatial resolution obtained in the images. The spatial resolution can be seen as the “detail” each image has and varies depending on ionization techniques; in some cases, it can be higher than 500 nanometers (nm), but it is typically found between 5 and 200  $\mu\text{m}$  [8]. MSI should only be used when spatial information is needed, as other techniques such as LC-MS and GC-MS are more sensitive and can be better used to quantify data if needed. MSI by itself is not the best option for drug detection as it does not allow for separation as in other more traditional bioanalysis. However, if spatial information is required, MSI is the best technique, and its numerous developments are making it more viable.

## 1.2 Ionization Techniques in Mass Spectrometry Imaging

It is imperative to ionize the molecules found in a sample to properly analyze them. A sample is ionized when its molecules are turned into charged particles. This process is usually done by adding or removing electrons from the atoms or molecules. Ionization is the most crucial step for MSI as it is imperative to properly separate ions based on their mass-to-charge ratios. While there are a lot of ionization techniques, the four most popular for MSI will be discussed and compared here.

### 1.2.1 Liquid Extraction Surface Analysis

Liquid Extraction Surface Analysis (LESA) is a soft ionization MS technique that works particularly well for analyzing whole proteins from a wide array of biological surfaces such as tissue sections. LESA has a lot of positive qualities such as the ability to analyze the intact protein rather than broken-down sections of it [9]. As a result, it is possible to get more details of the structure of the protein such as nucleotide polymorphisms and the presence and connectivity of genetic variations and post-translational modifications the target protein has gone through. LESA uses a conductive tip and the tissue sample to form a liquid juncture where the analytes of interest are extracted.

However, one of LESA's main issues is that the extracted sample is usually very chemically complex. As a result, LESA is usually coupled with ion mobility separation. For example, High Field Asymmetric Waveform Ion Mobility Spectrometry (FAIMS) can separate gas phase ions at atmospheric pressure by exploiting the differences in their mobilities at different electric field intensities [10]. In FAMIS, ions are passed through parallel electrodes, and an asymmetrical waveform is applied separating the ions by their ion mobilities. LESA has been used with MSI to provide special distribution of biological tissue. For example, Cooper et al., 2016 [3] used LESA FAIMS to spatially profile proteins from mouse liver and brain. They were able to find 40 protein species in the liver and 34 in the brain. The spatial distributions of proteins identified were in good

agreement with the literature meaning that LESA is a viable tool for MSI of proteins. Another big limitation that LESA has is the biological matrix, which can suppress important ions making its relative quantitation tricky [11]. As such, optimizing for the target proteins in the analyte is crucial, and usually consists of adjusting the solvent's volume, composition, and dwell time to improve the ionization of the target analytes.

Finally, by far the biggest limitation of LESA is its spatial resolution. Due to the sample's heavy and complex composition, it can only be optimized up to 1 mm making it not suitable for high-resolution imaging [12]. Even though recent developments such as Micro Liquid Extraction Surface Analysis ( $\mu$ LESA) have pushed the spatial resolution down to 400 nm, the resolution is still too low to compete with other ionization techniques [13].

### 1.2.2 Secondary Ion Mass Spectrometry

Secondary Ion Mass Spectrometry (SIMS) is a hard ionization technique, and the first ionization technique developed for MSI. In this method, a primary ion beam is directed towards the sample and bombards the sample surface (usually with ions such as  $\text{Ar}^+$ ,  $\text{Ga}^+$ , and  $\text{Cs}^+$ ) placed onto a glass slide or metal plate causing significant fragmentation of the sample molecules. This, in turn, generates secondary ions from the impact releasing atoms, molecules, and molecular fragments into the vacuum system as seen in **Figure 1.1** [14]. A portion of the liberated material is positively or negatively charged, subsequently being extracted into the detector, and separated based on its mass-to-charge ratio. SIMS has the advantage of achieving a high spatial resolution going down to 50 nm, which is lower than other MSI popular techniques. Like LESA, SIMS requires no matrix and thus reduces problems such as ion delocalization. Additionally, since SIMS uses ion beams and not a laser, it's able to image with greater accuracy going up to nanometers [15].

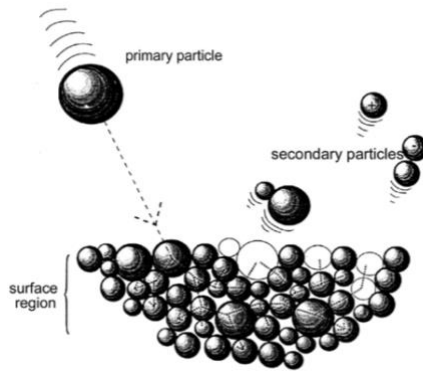


**Figure 1.1** Diagram of the SIMS process [15]

Recently, SIMS has been using different ions to bombard the sample, specifically, polyatomic ion beams such as  $C_{60}^+$  and  $(H_2O)_n$  [16, 17]. The main advantage of bombarding with polyatomic ions is an increase in ion yield and a reduction in sample damage [18]. This novel optimization of SIMS has made it a more popular technique than ever before.

However, SIMS has a lot of limitations. The main limitation of SIMS comes in its ionization process. The ion beam's energy often significantly damages the sample's chemical bonds and molecular structure. As a result, imaging without major molecular damage is limited to  $10^{13}$  ions/cm<sup>2</sup> [15]. The fragmentation can alter the sample composition, leading to inaccuracies in quantification, as some molecules are more prone to damage than others [19]. Another limitation can be found in the sample. Some samples are not conductive and, therefore, require a conductive coating, which can alter the sample composition or cause undesired reactions. Finally, most SIMS systems are complex and highly expensive making their accessibility significantly lower than other systems.

### 1.2.3 Desorption electrospray ionization mass spectrometry

Desorption electrospray ionization mass spectrometry (DESI) is a soft ionization technique that uses a spray of charged solvent to desorb the analytes and extract ions from the tissue. To facilitate the ionization process, the solvent passes through a charged capillary aided by a nebulizing gas (usually nitrogen or argon). [20] The sample is then bombarded by the charged solvent dissolving and accelerating the ions in the sample. As this happens, ions are desorbed from the sample and travel towards the mass analyzer through the inlet capillary. A DESI scheme can be seen in **Figure 1.2**. The resulting charged ions fly into the detector, which separates them based on their mass-to-charge ratio. DESI requires marginal pre-treatment but heavily relies on solvent choice to properly desorb and ionize analytes.

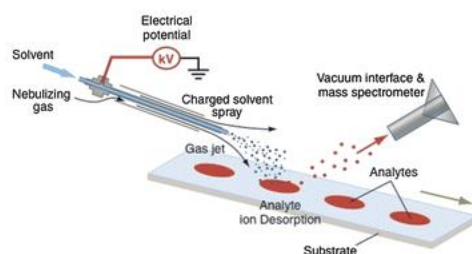


**Figure 1.2.** Schematic of operation of a normal DESI experiment [21]

In DESI, data is acquired in line scans instead of spots. As such, optimization of geometrical settings such as the angle and distance of DESI solvent and its inlet capillaries is a must as it dramatically improves the spatial resolution and reproducibility of DESI experiments [22]. Furthermore, DESI can improve its sensibility by derivatization. This is achieved by introducing the derivatizing agent to the solvent, aiding the ionization and analysis of hard-to-detect analytes. This is known as “reactive DESI”, and has seen extensive use for the detection of steroids in urine by reacting hydroxylamine with the steroid carbonyl groups [23]. One of the technique’s main challenges is its slow spatial resolution; even a fully optimized DESI cannot have a spatial resolution of more than 200  $\mu\text{m}$  (micrometers) [21]. However, it does not require a high vacuum and can be used without any prior sample preparation. As such, most of its applications are in forensic investigations and security stations for the screening of drugs. DESI is also not bound to any matrices, resulting in a very clean background signal with minimal interference.

A recent development of DESI, nano-DESI, drastically improves the spatial resolution to less than 12  $\mu\text{m}$  in tissue samples. The main modification involves the formation of a constant-flow liquid bridge between two capillaries meeting at the surface. The first capillary delivers the solvent to the sample, while the second one carries the washed analytes to the analyzer by generating a nano-electrospray. This reduces ion suppression as well as well as increasing the spatial resolution [24]. Nano-DESI is excellent for small molecules as its clean background allows it to work in the low mass range with ease. However, it faces challenges in proteomics as it struggles to ionize molecules in higher mass ranges. As a result, most nano-DESI MSI experiments of proteins are performed with a spatial resolution of 80  $\mu\text{m}$  [25]. These improvements are rapidly making DESI an attractive option for MSI, and it is quickly gaining popularity among researchers in the area.

#### 1.2.4 Matrix-Assisted Laser/ Desorption Ionization

Introduced in 1988 by Koichi Tanaka [26], Matrix-Assisted Laser/Desorption Ionization (MALDI) is the most popular and developed MSI technique. It is the most widely used ionization source thanks to its high availability and excellent capabilities in imaging proteomics and other large biomolecules. MALDI provides high mass range coverage, the ability to detect an extensive diversity of analytes, and a superb spatial resolution, being able to reach values under 10  $\mu\text{m}$  [27]. MALDI can analyze a wide array of molecules such as peptides, proteins, lipids, fatty acids, endogenous metabolites, and many more molecules with weights ranging from hundreds to thousands of Daltons (Da).

MALDI IMS consists of using a matrix that co-crystalizes analytes in a sample thaw mounted onto a sample plate, usually a glass slide or metal plate, followed by laser irradiation with an ultraviolet (UV) laser ranging from 335 to 349 nm in wavelength onto the sample's surface to ablate the matrix with the analytes [27, 28]. The matrix absorbs the high energy of the laser, aiding in the preservation of analyte molecules and their ionization. This causes the matrix-analyte crystal to desorb and ionize in the gas phase, as shown in **Figure 1.3**. The photoionization caused by this process generates primary ions from neutral molecules found in the sample. Additional secondary



ions are generated when more acidic matrices cause a “plume” by electron transfer once the molecules are in the gas phase near the detector [28].

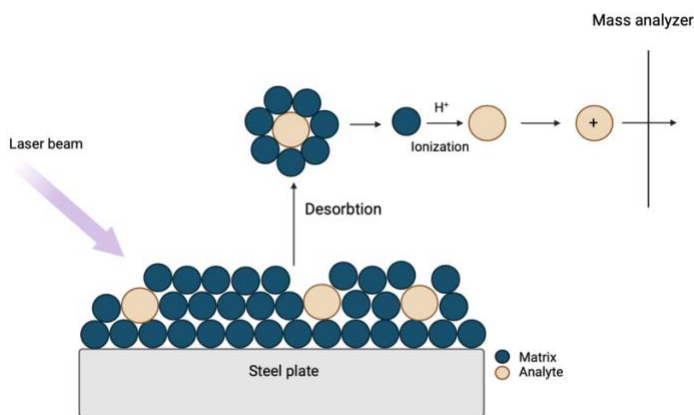


**Figure 1.3.** MALDI ionization process

Naturally, the instrument has positive and negative modes. In the former, molecules are protonated by attaching cations, usually producing  $[M + H]^+$  ions although ions such as potassium and sodium ions can be seen occasionally, yielding  $[M + Na]^+$  and  $[M + K]^+$  ion forms for sodium and potassium, respectively. In the latter, molecules are deprotonated yielding  $[M - H]^-$  ions.

The selection and deposition of the matrix are crucial as they have a drastic effect on the quality of results for each MALDI experiment. As such, it is imperative to find the best matrix for the specific group of target analytes that want to be explored. A good matrix must have the ability to absorb the wavelength applied by the laser, have minimal to no background signal in the desired mass range, have a strong ionization affinity with the selected analyte while preventing cluster formation, and have a consistent way to be applied onto the sample [29]. More on the matrix selection and its usage will be discussed further in this chapter. To further enhance the efficacy of targeted ionization, reactive matrices have developed chemical derivatization within organic groups to increase signal sensitivity. Another evidence of MALDI's great flexibility can be observed in the ambient ionization methods as they increase MALDI's speed and practicality

ditching the need for a high vacuum environment [30]. Because of its numerous advantages, MALDI is the best MSI source and will be discussed further in this work.

### 1.3 MALDI MSI for Small Molecules

As stated before, MALDI MSI has been the most common MSI technique since its introduction in the 1990s. MALDI has a strong presence for biological analysis as it works fantastic for the ionization and imaging of proteins, something other ionization techniques cannot provide easily [30].

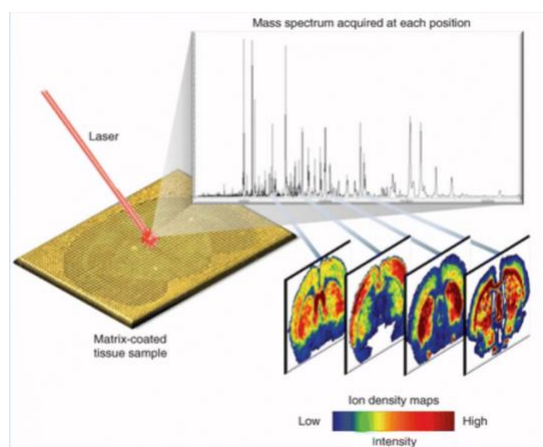


**Figure 1.4.** MALDI MSI scheme [3]

In MALDI MSI the mass spectra acquired over the tissue are defined by a laser step typically ranging from 10 to 100  $\mu\text{m}$ . Each pixel gives a new mass spectrum that is used to generate an image of the selected region as shown in **Figure 1.4**. The charge of the ions extracted into the mass analyzer is based on the type of voltage polarity, which can be controlled by the instrument [32]. To obtain the highest quality image, several MALDI MSI parameters must be optimized. The most important is the matrix. For small molecules, finding good matrices can be tricky as their low mass range is usually met with matrix peaks from most conventional matrices.

#### 1.3.1 Biological Tissue Preparation for MALDI

Most samples found in studies done by MSI come from *ex vivo* samples such as brain tissue and liver tissue. These types of samples must be put into a frozen state immediately to stop as many chemical and biological reactions as possible. Usually, putting samples in a  $-80\text{ }^{\circ}\text{C}$  freezer is

sufficient for most samples, as higher temperatures can cause the formation of ice crystals, limiting their imaging capabilities [33]. Another option is to put the samples on dry ice or liquid nitrogen until their further use.

Since it is not possible to image an entire organ, sectioning the sample is a common practice. Once the samples are ready to be used, they must be sectioned under a regulated temperature chamber, typically set to  $-17\text{ }^{\circ}\text{C}$ . This process is known as cryo-sectioning. When cryo-sectioning a frozen organ, frozen samples are cut into slices on a cryostat by repeatedly moving the sample toward the blade. The thickness of the tissue can range from 10 to 30  $\mu\text{m}$ . Because the sections tend to curl up, an anti-roll bar or glass plate is used to keep the sample flat until it is thaw-mounted onto an indium tin oxide (ITO) glass slide. Afterward, the glass slides are stored in the  $-80\text{ }^{\circ}\text{C}$  freezer again until it is time to image them. The cryo-sectioning process can be seen in **Figure 1.5**.

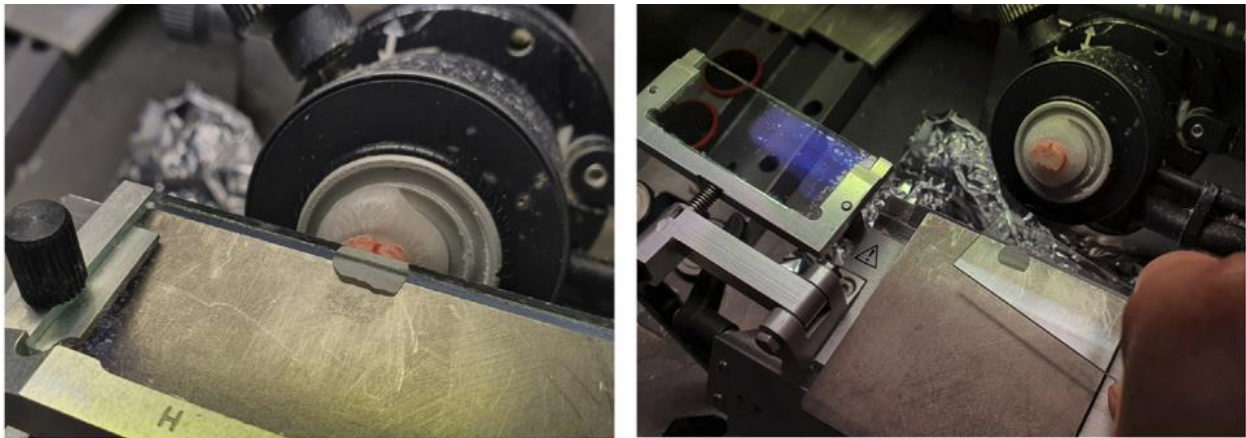


**Figure 1.5.** The cryo-sectioning of a mouse brain. The anti-roll bar prevents the cut sections from curling up (left). The section is thaw-mounted to an ITO glass slide and is stored at  $-80\text{ }^{\circ}\text{C}$  until used [34]

Several protocols of tissue preparation have been developed over time, including embedding the sample to maintain structural integrity during the sectioning. The embedded media is usually gelatin or carboxymethylcellulose. However, some studies have shown it to cause ion suppression in biological tissue [35] and thus not widely used.

### 1.3.2 Brief Overview of the Matrix in MALDI MSI

In MALDI, a matrix is any substance that can ionize analytes in a sample. As mentioned before, the matrix plays a central role in the MALDI process, aiding in the ionization and desorption of the target analytes. Therefore, for a successful MALDI experiment, it is key to choose an appropriate matrix for a specific sample [35]. Over the years, various matrices have been developed, such as  $\alpha$ -cyano-4-hydroxycinnamic acid (CHCA), 1,5-diaminophthalene (DAN), and 2,5-dihydroxybenzoic acid (DHB) to ionize different proteins, peptides, and other organic molecules [36-39].

Common organic matrices such as 2,5-dihydroxybenzoic acid (DHB) exhibit strong background signals in the low mass range (in the range of 150-250  $m/z$ ), hindering the detection of most neurotransmitters and other small molecules [40]. Consequently, using traditional organic matrices for small molecules remains challenging, leading to the development of novel matrices to address this issue. Additionally, the ionization efficiency of certain analytes can be hindered when they compete with matrix ions.

The main ionization mechanisms of MALDI matrices are charge or proton transfer and photoabsorption. In charge transfer, the matrix donates or accepts charge to or from an analyte molecule, which leads to the formation of charged ions through charged transfer processes. In proton transfer, protons are transferred from the matrix to the analyte, playing a significant role in the ionization process and producing positively charged ions. In photoabsorption, the matrix absorbs the energy, leading to rapid heating. This heat generates a highly energetic matrix plume, which goes to the detector. [41] As it can be noticed, the matrix plays the most crucial role in ionizing the sample and detecting the target analytes. More on matrix selection will be seen further in this chapter.

### 1.3.3 Matrix Deposition

Once the appropriate matrix has been selected, it is imperative to deposit the matrix properly onto the sample to ensure successful co-crystallization. Therefore, finding a method to uniformly apply it to the tissue to avoid hot spots and obtain high-quality images. When the process is done correctly, small crystal sizes caused by the matrix will result in a high spatial resolution while preventing analyte delocalization. Analyte delocalization occurs when the analyte is washed away from its original position, leading to a broadened ion signal in the mass spectrometer, decreased spatial resolution, and lower-quality ion images. An effective method must prevent analyte delocalization and enable the formation of small crystals in a reproducible and efficient manner.

Four main methods have been developed for this task. The first and most economical method is using an airbrush. In this approach, the matrix is sprayed onto the sample using an aerosol sprayer or airbrush from a specific distance. However, it requires technical skill to achieve the appropriate coating of the sample with the right amount of matrix, and its reproducibility is limited since it relies on individual users, making it prone to variations [42].

The second method follows a similar concept as the manual airbrush, but it involves an automatic sprayer. This automated technique allows for better reproducibility as it enables precise control of parameters such as the solvent flow rate, nozzle velocity, temperature, and the number of passes. Commercially available automatic sprayers like ImagePrep (Bruker Daltonics), SunCollect (SunChrom), and TM-Sprayer (HTX Technologies) offer this advantage and can also spray enzyme solutions and standards for on-tissue experiments [43].

Another wet technique is micro-spotting, where matrix droplets are deposited on specific spots on the tissue. Devices like the Jet Printer (Shimadzu) are available commercially, providing a uniform coating of matrix enzyme solutions. However, the use of matrix droplets may result in a lower

spatial resolution compared to automatic sprayers, making them less suitable for certain applications.

Finally, sublimation is a dry deposition method conducted under high temperatures. The sample is mixed with a suitable solvent and allowed to evaporate, leaving a solid matrix coating. Sublimation offers the advantage of preventing analyte delocalization as it is a solvent-free method, providing high spatial resolution for metabolites and lipids [43]. This technique produces very fine crystals, but its application is limited to specific matrices with a low evaporating point.

#### 1.3.4 Spatial Resolution, Ion Selectivity and Sensitivity

Several parameters influence the spatial resolution in MSI images. As mentioned earlier, the size and uniformity of the matrix crystals are critical factors. The matrix crystal size needs to be smaller than the raster step size. If the crystal size exceeds the raster step size, oversampling may occur, where multiple raster steps cover a single large matrix crystal. Oversampling can also happen if the laser raster step size is smaller than the laser beam size [44]. This results in inaccurate and redundant information, leading to an image that does not fully represent the true spatial resolution of the analyte.

Moreover, having a high-quality mass spectrometer instrument with advanced ion optics and detectors enhances the resolution capabilities, sensitivity, and selectivity, leading to better spatial resolution in the MSI data. Another critical parameter is the laser spot size. Smaller laser spots can achieve higher resolution by focusing on specific regions of the sample with greater precision.

It's important to consider that time can also be a significant factor in comprehensive studies. In certain cases, the highest spatial resolution may not be necessary and could be compromised for a

faster scan time. Efficient resource management is required to balance the image quality with the resources used to obtain them, such as laser time, to ensure optimal results in MSI experiments.



## 1.4 Mass Analyzers for MSI

After the sample has been ionized, mass analyzers are used to separate the ionized gas-phase ions by their mass-to-charge ratios. In MALDI MSI, the most common analyzers are time-of-flight (TOF), Fourier-transform ion cyclotron resonance (FT-IRC), and Orbitrap. A good mass analyzer has high resolving power, speed, sensitivity, and wide mass range. Like MS sources, there is no perfect mass analyzer, and they all have different advantages and disadvantages.

### 1.4.1 Mass Accuracy and its Meaning for MALDI MSI

Before discussing the different mass analyzers, it is essential to understand the impact of mass accuracy in the functioning of mass spectrometers. As such, mass resolving power is a critical parameter used to quantify the ability of a mass spectrometer to distinguish between two ions with different  $m/z$  values [45]. Resolving power characterizes the performance of a spectrometer or the degree to which a laser beam is monochromatic. It can also be seen as the “valley” between two peaks. This definition can be expanded and used to obtain the resolution ( $R$ ) of any system, as seen in equation 1.1.  $\Delta(m/z)$  is the width of the peak at 50% of its peak height, while  $m/z$  indicates the peak position. Naturally, the narrower the peak ( $\Delta(m/z)$ ) the higher the resolution will be.

$$R = \frac{m/z}{\Delta(m/z)} \quad \text{Eq. 1.1.}$$

To provide a practical example, if a mass spectrometer has a resolving power of 10,000 at 400  $m/z$ , it means that it can distinguish ions with  $m/z$  values differing by 0.05 Da at 400  $m/z$ . A high resolving power is always preferred as it allows for the identification and characterization of different biomolecules, especially in the cases of similar masses. It also enables scientists to properly distinguish between isotopic peaks in complex spectra.

On the other hand, mass accuracy determines how closely the measured mass of an ion corresponds to its true mass. It is a parameter used to quantify both precision and reliability of a mass spectrometer apparatus. Mass accuracy is measured in parts per million (ppm). A low ppm means

that the spectrometer is highly accurate and reliable. To calculate mass accuracy, it is possible to use the formula in equation 1.2.

$$\text{Mass Accuracy} = \frac{\text{Measured Mass} - \text{True Mass}}{\text{True Mass}} \times 1,000,000 \quad \text{Eq. 1.2.}$$

Both parameters can be increased with better mass analyzers and detectors, which will be discussed next.

#### 1.4.2 Time-of-Flight (TOF) Analyzer

A Time-of-Flight (TOF) analyzer relies on the free flight of ionized molecules in a two-meter tube before reaching the detector. Its principle stems from the fact that if two ions with the same charge are formed at the same time, the one with the higher mass will reach the detector first [45]. In a TOF analyzer, all ions will reach the detector at a certain point. It can also detect ions in a very high mass range, but it has the major downside of the linearity of the tube. As ions entering the tube often carry varying kinetic energy, resolving power and mass accuracy are often compromised. However, this downside can be resolved by the installation of a reflectron. A reflectron is an ion mirror that generates an electrical field and repels ions based on their kinetic energy. The higher their kinetic energy, the more the ion will be slowed down. As a result, the mass spectrum obtained will have narrower and better-resolved ion peaks, thus improving the mass resolution and accuracy of the instrument [46]. However, some ions can be lost due to the inclusion of a reflectron, although the operator can choose whether to use it to improve resolution or not to improve selectivity. The linear TOF and reflectron schemes can be found in Figure 1.6. Another way to improve ion resolution is to make the TOF path longer. Because ions travel a longer distance, it is easier to separate between masses, giving a higher resolving power.

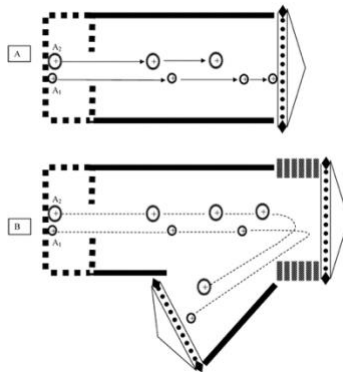


**Figure 1.6.** A) A traditional linear TOF path where  $A_2$  and  $A_1$  are ions with different masses and kinetic energies. B) A reflectron TOF path where  $A_2$  and  $A_1$  are ions with different masses and kinetic energies [45].

#### 1.4.3 Fourier-Transform Ion Cyclotron Resonance Analyzer

The Fourier-Transform Ion Cyclotron Resonance Analyzer (FT-IRC) is a high-resolution mass analyzer that offers superb mass accuracy. It is one of the most advanced mass analyzers and can provide extremely high mass resolution, accuracy, and sensitivity. In an FT-IRC detector, ions are trapped in a strong magnetic field generated by the detector. This field causes the ions to spiral in a circular path under a specific frequency, which is known as the cyclotron frequency. The cyclotron frequency is specific to each ion, as it is determined by its  $m/z$  and the strength of the magnetic field.

As ions oscillate, they induce a current in the detector plates exciting them to higher levels. The level of these currents is measured over a certain period and creates an interferogram which is subjected to Fourier-transform analysis. The Fourier transform decomposes the interferogram into frequencies which are used, in conjunction with the magnetic field strength to calculate the ion masses by the system. A scheme of an FT-IRC mass analyzer can be found in **Figure 1.7**.

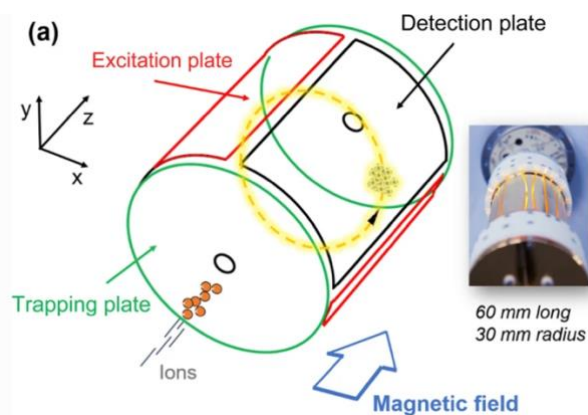


**Figure 1.7.** Schematic diagram of FT-ICR mass analyzer (left) and the actual picture of the cylindrical cell of one (right) [47]

As previously mentioned, FT-IRC systems offer high mass resolution and accuracy, giving mass accuracies of less than 1 ppm. They are also highly sensitive, enabling them to detect low-abundance analytes in complex biological standards. However, FT-IRC analyzers can suffer from a long analysis time, which is why commercial ones are often equipped with other mass analyzers. They can also be very expensive in comparison to other mass analyzers.

#### 1.4.4 Orbitrap analyzer

The Orbitrap mass analyzer consists of three electrodes, where two outer electrodes in the form of a cup face each other. These electrodes are electrically isolated and aligned to a central electrode. This setup works like a trap. When voltage is applied between the outer and central electrodes, the resulting electric field is strictly linear along the axis and oscillates harmonically. Simultaneously, the radial component of the field starts to attract ions to the central electrode [48]. The ions are trapped in the space between the outer and inner electrodes. The voltage applied causes the radial field to bend the trajectory towards the central electrode, creating a centrifugal force. The ions will remain in the electric field on a nearly circular spiral inside the trap, like planets in a solar system. Then, the outer electrodes act as a receiving plate for the image current of the motion of the ions. This current is subjected to a Fourier-transform analysis, like the FT-ICR analyzer, to obtain a mass spectrum.

Orbitrap analyzers possess high mass resolution with a mass accuracy of less than 5 ppm. However, they have trouble with high masses ( $< 4000 m/z$ ) as their rotation can be difficult to keep in orbit. Orbitrap analyzers are usually coupled with FT-IRC analyzers to compensate for the high analysis time the former takes.

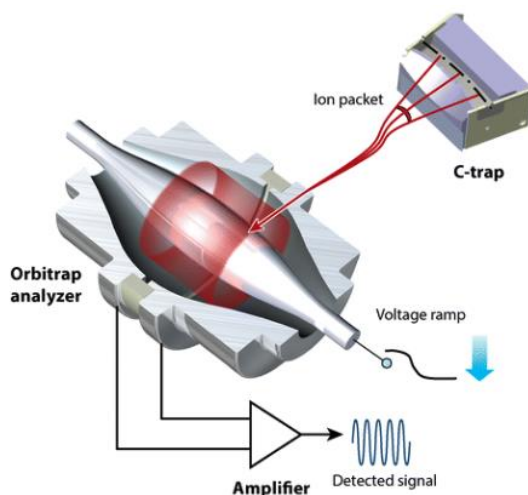


**Figure 1.8.** Diagram of a typical Orbitrap mass analyzer [48]

#### 1.4.5 MS Detector

To assess the quantity of each ion species separated by  $m/z$ , we use MS detectors. In the case of FT-IRC and Orbitrap, these analyzers themselves serve as MS detectors. However, for TOF a separate detector is needed. An ideal detector should have unity ion efficiency, virtually no noise, stability under vacuum, a wide mass range, dynamic range, fast response, and high saturation level [49]. There is no perfect MS detector, and the one that best suits the specific needs of the analyzer must be used. In the case of a TOF analyzer, rapid response, recovery, and a wide dynamic range are prioritized. The most popular MS detectors include the Faraday cup, the electron multiplier, and the photomultiplier [50]. A typical detector generates a low ion current from the source through the analyzer to the detector, which is then converted to an electric current. Finally, this current is amplified and digitalized into data.

## 1.5 Matrices in MALDI for Small Molecule Detection

Small metabolites, such as drugs, neurotransmitters, amino acids, and various other compounds, often have limited ionization efficiency when directly subjected to MALDI. Therefore, the presence of a strong matrix is imperative to significantly improve the ionization process, allowing for the generation of ion signals for MALDI analysis. As mentioned earlier, working in the low mass range poses a significant challenge for most matrices due to their strong peaks in this area.

There are three different types of matrices commonly used for small molecule detection in MALDI: reactive matrices, organic matrices, and metal and metal oxide nanomaterials. Reactive matrices can undergo a chemical reaction with the target analytes, resulting in enhanced ionization. Organic matrices, which are traditionally used for higher molecular weight molecules, have characteristic peaks that make them less ideal for small molecule detection and are consequently the least used matrices in this context. On the other hand, nanomaterials made of metals and metal oxides show promise as matrices for small molecule detection in MALDI due to their unique characteristics, making them an intriguing material to work with in this application.

### 1.5.1 Matrix Selection for Small Molecules

Matrix selection is often an empirical process, where researchers test several matrices to optimize ionization efficiency and sensitivity for a specific set of molecules. These tests are usually first done using molecular standards, where each standard is spotted onto a metal plate in conjunction with the matrix. Then, the laser is used to analyze the obtained signals from the standards-matrix mixture. This process can be repeated several times with varying concentrations to plot a calibration curve and optimize matrix concentration. Afterward, the experiment is repeated using biological tissue, as sometimes the nature of the spot can give misleading results. On tissue, a more complex spectrum should be expected, as multiple ions are competing for the ionization produced by the matrix [51]. Additionally, effects such as ion suppression and delocalization must be considered when evaluating the potential of a matrix.

The main considerations and factors to keep in mind when selecting a matrix are compatible background interference, sensitivity, selectivity, and dynamic range. The matrix should also be readily soluble in a suitable solvent to prepare a homogeneous matrix-analyte mixture in the sample. The matrix's ionization mechanism should also be taken into consideration, as it can affect the ionization efficiency. Finally, signal suppression has been reported by different matrices for several molecules [52-54], so it is important to ensure that no signal interference occurs between the target molecule and matrix for accurate quantification and identification.

### 1.5.2 Ionization Methods Among Different Matrices.

Challenging analytes with low ionization efficiencies are not easily detected by MALDI. Another issue that small molecules have is that certain mass analyzers, such as TOF, have a hard time detecting these types of molecules. Several ionization methods can be used to tackle these problems. One of the most popular ones is chemical derivatization (CD). CD is a targeted ionization technique where the target molecule reacts through the functional groups of a chemical reagent with the matrix in use.

CD has been demonstrated as a viable technique for different mass spectrometry techniques, such as imaging platforms like MALDI and DESI [55-56]. For biological samples, CD is often called on-tissue chemical derivatization (OTCD). While OTCD is a great specific approach to ionizing target molecules, it comes with its own set of drawbacks. For starters, unwanted side reactions can occur, giving additional background interference. Also, the risk of delocalization and even loss of analyte can be a major concern for small molecules. There's also an increased sample preparation challenge as the sample surface is "wetted" with the derivatizing agent, causing ion delocalization [57]. Finally, additional incubation/reaction times and increased temperature may be needed to properly verify the full chemical reaction has taken place. As a result, the choice of matrix, chemical reagent, and deposition method must be heavily optimized to prevent these drawbacks.

Another ionization technique commonly found in matrices is charge transfer. In the context of MALDI, charge transfer occurs when an ionic or polar matrix interacts with a neutral analyte in

the sample. During the MALDI process, the matrix absorbs the laser energy and becomes excited. The excited matrix transfers an electron to the co-crystallized analyte, giving a charged analyte ion. This ionization mechanism is often seen in large molecules such as peptides or proteins. Since charge transfer is a soft ionization technique, minimal fragmentation occurs, which preserves the spatial integrity of the sample and can be used as an additional validation point for structural identification. The main disadvantage of charge transfer is its low ionization efficiency [58]. Small or non-polar compounds may have lower ionization yields, leading to low or no sensitivity, which is the case for many small molecules. Additionally, although no major fragmentation happens in most molecules, in some cases such as lipids and fatty acids, fragmentation between the head group and the tail hinders its ability to properly quantify these analytes [59].

Finally, if the matrix has heat-absorbing and conductive properties, the matrix ionization can be thermally driven, also known as photoabsorption. While this mechanism is not entirely understood, the matrix desorbs the analyte molecules from the sample, and the heat energy further promotes ionization, leading to gas-phase ions. This is a very gentle ionization mechanism offering good sensitivity. However, since it depends mainly on heat, it offers low selectivity as many analytes ionize at the same rate. This can be a limiting factor for the detection of low-abundance analytes. The matrices that exhibit this ionization mechanism have a relatively high surface area, which means most of them are nanometric.

### 1.5.3 Reactive Matrices for Small Molecule Detection

As mentioned before, chemical derivatization is a well-established strategy for the detection of small molecules. Through the derivatization of amino groups of different metabolites, OTCD can effectively yield great ionizing results. There are four main reagents used for the derivatization of small molecules.



The first one is p-N, N, N-trimethylammonioanilyl N-hydroxysuccinimidyl carbamate iodide (TAHS). TAHS can be pneumatically sprayed using 70% acetonitrile (ACN) as solvent. The derivatizing reagent is sprayed after the matrix (usually DHB) and is incubated overnight at 55 °C to suppress any undesired side reactions between THAS and phenolic hydroxyl groups [60]. THAS forms positively charged derivatives that enable the analysis of small molecules such as neurotransmitters (NTs) and amino acids. Without the addition of a matrix, TAHS's ability to detect analytes is greatly compromised as noted by Esteve, et al. At a concentration of 30 mg/mL, TAHS can detect 19 different small molecules most of them consisting of amino acids and neurotransmitters [61]. Some notable molecules that are detected by this matrix include Glycine,  $\gamma$ -aminobutyric acid (GABA), Taurine, Glutamine, Glutamate, and Dopamine.

Another chemical reagent is 4-hydroxy-3-methoxycinnamaldehyde (CA). Similarly, to TAHS, a matrix is previously sprayed before the application of the reagent, in this case, Trans-Ferulic Acid or DHB [61-63]. An overnight incubation period at 37 °C is sufficient to yield a good reaction while avoiding unwanted side reactions [62]. In a rat brain tissue, CA was able to detect 24 different small molecules. The list includes important NTs such as GABA, Serotonin, and Dopamine, and important amino acids such as Alanine and Histidine [61].

The third chemical reagent is 2,3-diphenyl-pyranylium tetrafluoro-borate (DPP-TFB). DPP-TFB requires an additional matrix, which can either be CHCA or DHB [61, 64]. It is stored at room temperature with an overnight incubation period. After the reaction is completed, DPP-TFB can detect 19 small molecules including Serotonin, 3-MT, Glutamate, GABA, and Tyramine. These three matrices target the amine group in the target molecules and are thus very versatile for the detection of amino acids. The reaction mechanisms of these three molecules can be found in **Figure 1.9**.

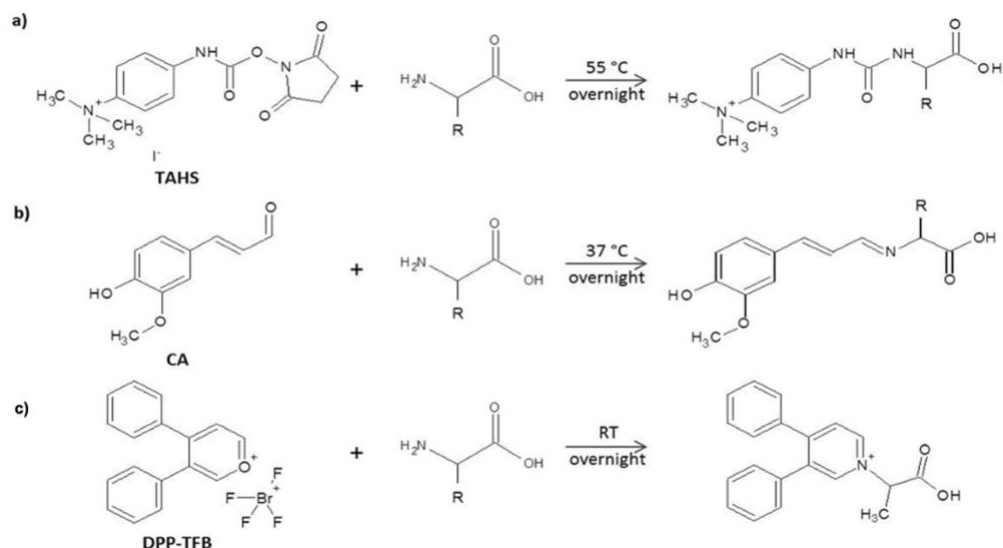


**Figure 1.9.** Reaction mechanism of a) TAHS, b) CA, and c) DPP-TFB [61].

The final chemical reagent is 4-(anthracene-9-yl)-2-fluoro-1-methylpyridin-1-ium iodide (FMP-10). FMP-10 was developed by P. E. Andren and is the last reagent in the list of fluoromethylpyridinium-based reactive matrices. FMP-10 facilitates the covalent charge-tagging of molecules that have phenolic hydroxyl or primary/secondary amine groups, which include serotonergic and dopaminergic metabolites [65]. The results can yield resolutions of 10  $\mu\text{m}$ . Unlike other reagents, FMP-10 does not require a separate matrix and acts as the matrix itself. FMP-10 is commercially available and is widely used for a lot of different applications such as liver imaging [66], and mouse brain [67], among other applications. FMP-10 is chemically designed to incorporate two functional domains, one highly electrophilic fluoropyridinium moiety, which facilitates covalent analyte charge-tagging, and one conjugated chromophore domain, which promotes laser desorption, as seen in **Figure 1.10**. Most molecules can be detected in single-derivatized, doubly-derivatized, and triply-derivatized ion forms with varying intensities for each form [65].

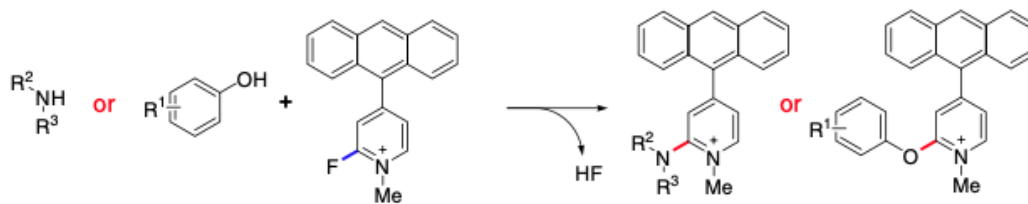


**Figure 1.10.** Schematic of the reaction between the FMP-10 matrix and phenolic hydroxyls and amines [65]

FMP-10 can detect up to 31 small molecules, most of them being NTs and amino acids. The list includes the previously mentioned Dopamine, Serotonin, Lysine, GABA, Creatinine, Arginine, and many more [65]. However, it is important to note that the analytes detected can vary with different instruments, mass analyzers, and detectors.

#### 1.5.4 Organic Matrices for Small Molecule Detection

Although harder to use due to their strong background peaks, some organic matrices have proven to have ionizing effects for small molecules. For example, CHCA has often been cited as a strong ionizing organic compound although its matrix peaks prevent it from detecting a lot of important molecules. For instance, CHCA is known to have a strong cluster ion peak around the 146  $m/z$  region making it impossible to work at such mass ranges. One way to overcome this problem is to work with deuterated CHCA ( $D_4$ -CHCA) as a matrix. This facilitates the imaging of small molecules such as acetylcholine and alpha-GPC, both important molecules found in the brain [68]. However,  $D_4$ -CHCA is very expensive and challenging to synthesize, which limits the use of this matrix for niche applications.

Another example is 1,5-Diaminonaphthalene (DAN), which is a matrix that usually uses lipids. However, despite its strong background peaks, it can efficiently work in the low mass range for certain molecules. As such, DAN has been used to directly visualize different small metabolites in

ischemic stroke brains treated with various drugs by Sun *et al.* [69]. In this study, DAN was able to detect 17 different compounds such as Glutamate, ATP, AMP, Citric Acid, and Aspartate.

Finally, 3,4-Dimethoxycinnamic Acid (DMCA) is a novel matrix with low matrix-ion-related interferences in the low mass range region and a strong ultraviolet absorption. DMCA has been used to image rat livers, rat brains, and even seeds [70]. DMCA is dissolved in a mixture of ACN and TFA and is sprayed directly onto the sample. DMCA's strong wavelength absorbance at 355 nm makes it a good matrix able to detect 6 different amino acids, including galactaric acid, phosphocholine, and cyclocreatine [70].

#### 1.5.5 Metals and Metal Oxide Nanoparticles for Small Molecule Detection

Metallic NPs have a high surface area, are stable in a vacuum, and exhibit good laser absorption in the Ultraviolet (UV) region. Although the ionization process between metal oxide nanoparticles (NP) matrices and metabolites is not fully understood, it appears to be thermally driven [71-72]. Laser irradiation heats the matrix, leading to the desorption of analytes in the organic tissue [71-72]. Therefore, a low heat conductivity of the matrix is preferred as it minimizes the diffusion of thermal energy [73]. Another question that has not been fully answered is the impact of the size of the NP matrices on MALDI signals. It is known that the optical properties of metallic NP are commonly related to their sizes. It is theorized that smaller NP provide greater desorption/ionization efficiency, leading to greater sensitivity. However, the size of the NP also affects their stability in sample solutions, meaning smaller-sized NPs may lead to irreproducibility due to their instability [73]. Additionally, metallic elements have specific affinities to different chemical structures. For example, it is known that Ag NP have a strong affinity for conjugating with double bonds [74], making them strong candidates for MSI analysis of carotenoids, olefins, and fatty acids [75]. Au NP have a high affinity for thiol groups due to the strong bonding of gold-sulfur (Au-S) [74]. However, the direct relationship between NP and different analytes has not been thoroughly studied, specifically for MALDI-MSI.

However, this doesn't mean that metallic NPs come without their own set of challenges. It is commonly known that metallic NPs easily aggregate, which is usually alleviated by using surface modification of the nanoparticles in the dispersant agent with surfactants such as PEG [73-75]. However, most of these capping agents can easily detach during the MALDI-MSI process, provoking signal contamination and substantial ion suppression of certain analytes. Naturally, it is difficult to combat aggregation without using capping agents. Several capping alternatives have been found that induce minimal disruption of the signal such as functionalized Dopamine-capped TiO<sub>2</sub> NPs [75] for neurotransmitter imaging in rat brains. As a result, the overall adoption of nanomaterials in the MSI community remains relatively sparse, as their specialized application methods and inconsistencies make these types of materials challenging to work with.

## 1.6 Conclusion

As shown throughout this chapter, MALDI MSI is a promising analytical tool that can relatively quantify the amount of different small molecules in tissue. It offers high sensitivity, selectivity, and ionization efficiency while preserving spatial integrity, making it an excellent choice for addressing biological and analytical questions. Various mass analyzers and ionization techniques were reviewed, showcasing the advantages and disadvantages of MALDI MSI. Additionally, a detailed flowchart of the sample preparation and its challenges was presented to illustrate the specific obstacles typical of MALDI MSI experiments. Furthermore, different matrices for the detection of small molecules were discussed, along with various chemical methods that aid in the ionization of hard-to-detect molecules found in biological samples.

The challenges in small molecule detection using MALDI MSI are significant, yet exciting. As demonstrated in this chapter, one of the major issues for detecting small molecules is finding a matrix capable of detecting them without introducing matrix signals or requiring additional chemical processes. The next chapter will delve into this search further, while Chapter 3 will explore a direct biological application of the optimized matrix to evaluate its effectiveness in detecting small molecules.

## 1.7 References

- [1] Falkowska, A.; Gutowska, I.; Goschorska, M.; Nowacki, P.; Chlubek, D.; Baranowska-Bosiacka, I. *International Journal of Molecular Sciences* **2015**, *16*, 25959-25981.
- [2] Adibhatla, R. M., and J. F. Hatcher. *Journal of Neuroscience Research* **2000**, *70*(2):133–139.
- [3] Milman, B. L. *TrAC Trends in Analytical Chemistry* **2015**, *69*, 24-33.
- [4] Lifshitz, C., & Laskin, J. (Eds.). *John Wiley & Sons*. **2006**, **580**, 130-135
- [5] Gowda, G. A. N.; Djukovic, D. *Methods in molecular biology* **2014**, *1198*, 3-12.
- [6] Zhang, X. W.; Li, Q. H.; Xu, Z. D.; Dou, J. J. *RSC Advances* **2020**, *10*, 3092-3104.
- [7] Granborg, J. R., Handler, A. M., & Janfelt, C., *TrAC Trends in Analytical Chemistry* **2022**, *146*, 116482.
- [8] J.G. Swales, G. Hamm, M.R. Clench, R.J. Goodwin, *Int. J. Mass Spectrom* **2019**, *437* 99-112.
- [9] Zhang, X., Na, N., & Ouyang, J., *TrAC Trends in Analytical Chemistry* **2021**, *143*, 116366.
- [10] Griffiths, R. L., Hughes, J. W., Abbatiello, S. E., Belford, M. W., Styles, I. B., & Cooper, H. *J. Analytical chemistry* **2020**, *92*(4), 2885-2890.
- [11] Griffiths, R. L.; Creese, A. J.; Race, A. M.; Bunch, J.; Cooper, H. J., *Anal. Chem.* **2016**, *88*, 6758–6766.
- [12] Eikel D, Vavrek M, Smith S, Bason C, Yeh S, Korfmacher WA, Henion JD., *Rapid Commun Mass Spectrom.* **2011**, *3587–3596*.
- [13] Yutuc E, Angelini R, Baumert M, Mast N, Pikuleva I, Newton J, Clench MR, Skibinski DOF, Howell OW, Wang Y, Griffiths WJ., *Proc Natl Acad Sci USA.* **2020**, *5749–5760*.
- [14] Vickerman, J. C., *ToF-SIMS: surface analysis by mass spectrometry* **2001**, 1-40.
- [15] Hammond, J.S., *Springer*, **2010**, 69-79
- [16] Chang CJ, Chang HY, You YW, Liao HY, Kuo YT, Kao WL, Yen GJ, Tsai MH, Shyue JJ., *Anal Chem Acta.* **2012**, *718*:64–69.
- [17] Kaya I, Brülls SM, Dunevall J, Jennische E, Lange S, Martensson J, Ewing AG, Malmberg P, Fletcher JS., *Anal Chem.* **2018**, *90*(22):13580–13590.
- [18] Sheraznée Rabbani S, Razo IB, Kohn T, Lockyer NP, Vickerman JC., *Anal Chem.* **2015**, *87*: 2367–2374.

- [19] Massonnet, P., & Heeren, R. M., *Journal of Analytical Atomic Spectrometry* **2019**, 34(11), 2217-2228.
- [20] Wu, C., Dill, A. L., Eberlin, L. S., Cooks, R. G., & Ifa, D. R., *Mass spectrometry reviews* **2013**, 32(3), 218-243.
- [21] Vickerman, J. C., *Analyst* **2011**, 136(11), 2199-2217.
- [22] Tillner J, Wu V, Jones EA, Pringle SD, Karancsi T, Dannhorn A, Veselkov K, McKenzie JS, Takáts Z., *J Am Soc Mass Spectrom.* **2015**, 28(10):2090–2098.
- [23] Huang G, Chen H, Zhang X, Cooks RG, Ouyang Z. *Analytical Chem.* **2007**, 79(21):8327–8332.
- [24] Yin R, Kyle J, Burnum-Johnson K, Bloodsworth K, Sussel L, Ansong C, Laskin J., *Analytical Chemistry*. **2018**, 90(11), 6548-6555.
- [25] Laskin, J., *Angewandte Chemie International Edition* **2022**, 61(29), e202200721.
- [26] Tanaka, K., Waki, H., Ido, Y., Akita, S., Yoshida, Y., Yoshida, T., & Matsuo. *Rapid communications in mass spectrometry*. **1998**, 2(8), 151-153.
- [27] Rohner, T. C., Staab, D., & Stoeckli., *Mechanisms of Ageing and Development* **2005**, 126(1), 177–185.
- [28] Dreisewerd K., *Chem Rev.* **2003**, 103(2):395–425.
- [29] Leopold J, Popkova Y, Engel KM, Schiller J., *Biomolecules* **2018**, 8(4):173.
- [30] Yin R, Burnum-Johnson KE, Sun X, Dey SK, Laskin J., *Nat Protoc.* **2019**, 14(12):3445–3470.
- [31] R.M. Caprioli, T.B. Farmer, J. Gile., *Anal. Chem.* **1997**, 69 4751e4760.
- [32] Zhang, S., Chen, Y., Xiong, S., Wang, G., Chen, J., & Yang, G., *Journal of the American Society for Mass Spectrometry*, **2010**, 21(1),154-160.
- [33] Good, C. J., Neumann, E. K., Butrico, C. E., Cassat, J. E., Caprioli, R. M., & Spraggins, J. M., *Analytical Chemistry* **2022**, 94(7), 3165-3172.
- [34] Granborg, J. R., Handler, A. M., & Janfelt, C., *TrAC Trends in Analytical Chemistry* **2022**, 146, 116482.
- [35] K.A. Nelson, G.J. Daniels, J.W. Fournie, M.J. Hemmer, *J. Biomol. Tech.: J. Biochem.* **2013**, 24, 119.
- [36] M. Karas, D. Bachmann, F. Hillenkamp, *Anal. Chem.* **1985**, 57, 2935– 2939.
- [37] Wylie, L. Chui, G. Westmacott, B. Xu, M. Drebot, C. Nadon, J. D. Knox, G. Wang, K. Chenga, J., *Clin. Microbiol.* **2015**, 53, 2480–2485.



- [38] J. Wang, G. Jiang, T. Vasanthan, P. Sporns., *Starch/Staerke*, **1999**, 51, 243–248.
- [39] M. Mank, B. Stahl, G. Boehm., *Anal. Chem.* **2004**, 76, 2938–2950.
- [40] Teearu, A.; Vahur, S.; Haljasorg, U.; Leito, I.; Haljasorg, T.; Toom, L., *Journal of Mass Spectrometry* **2014**, 49, 970-979.
- [41] Zhou, Q., Fülöp, A., & Hopf, C., *Analytical and bioanalytical chemistry* **2021**, 413, 2599-2617.
- [42] Lee, P. Y., Yeoh, Y., Omar, N., Pung, Y. F., Lim, L. C., & Low, T. Y., *Critical reviews in clinical laboratory sciences* **2021**, 58(7), 513-529.
- [43] Hankin, J. A., Barkley, R. M., & Murphy, R. C., *Journal of the American Society for Mass Spectrometry* **2007**, 18(9), 1646-1652.
- [44] Metodiev, M. D., Steven, R. T., Loizeau, X., Takats, Z., & Bunch, J., *Analytical Chemistry*, 93(46), **2021**, 15295-15305.
- [45] Murray, K. K., *Journal of the American Society for Mass Spectrometry* **2022**, 33(12), 2342-2347.
- [46] Mamyrin, B. A., *International Journal of Mass Spectrometry* **2001**, 206(3), 251-266.
- [47] Qi, Y., Xie, Q., Wang, J. J., He, D., Bao, H., Fu, Q. L., ... & Fu, P., *Carbon Research* **2022**, 1(1), 3.
- [48] Zubarev, R. A., & Makarov, A., *Orbitrap mass spectrometry* **2013**, 5288-5296
- [49] (97) Koppelaar, D. W.; Barinaga, C. J.; Denton, M. B.; Sperline, R. P.; Hieftje, G. M.; Schilling, G. D.; Andrade, F. J.; Barnes, J. H., *Analytical Chemistry* **2005**, 77, 418A-427A.
- [50] Greaves, J.; Roboz, J., *CRC Press* **2013**
- [51] Kobylis, P., Stepnowski, P., & Caban, M., *Microchemical Journal* **2021**, 164, 105983.
- [52] Qiao, Z., & Lissel, F., *Chemistry—An Asian Journal* **2021**, 16(8), 868-87
- [53] Tobias, F., & Hummon, A. B., *Journal of proteome research* **2020**, 19(9), 3620-3630.
- [54] Bastrup, J., Birkelund, S., Asuni, A. A., Volbracht, C., & Stensballe, A., *Rapid Communications in Mass Spectrometry* **2019**, 33(22), 1711-1721.
- [55] Cobice DF, Livingstone DEW, McBride A, MacKay CL, Walker BR, Webster SP, Andrew R., *Biochem Pharmacol.* **2018**,148: 88–99.
- [56] Girod M, Shi Y, Cheng JX, Cooks RG., *Analytical Chemistry* **2012**, 83(1):207–215.
- [57] Zhou, Q., Fülöp, A., & Hopf, C., *Analytical and bioanalytical chemistry* **2021**, 413, 2599-2617.

- [58] Karas, M., & Krüger, R., *Chemical Reviews* **2003**, *103*(2), 427-440.
- [59] Bae YJ, Kim MS., *Analytical Chemistry* **2015**, 2015;8:41-60.
- [60] Toue, S., Sugiura, Y., Kubo, A., Ohmura, M., Karakawa, S., Mizukoshi, T., et al., *Proteomics* **2014**, *14*, 810–819.
- [61] Esteve, C., Tolner, E. A., Shyti, R., van den Maagdenberg, A. M., & McDonnell, L. A., *Metabolomics* **2016**, *12*, 1-9.
- [62] Manier, M. L., Spraggins, J. M., Reyzer, M. L., Norris, J. L., & Caprioli, R. M., *Journal of Mass Spectrometry*, **2014**, *49*(8), 665-673.
- [63] Guo, S., Tang, W., Hu, Y., Chen, Y., Gordon, A., Li, B., & Li, P., *Analytical chemistry* **2019**, *92*(1), 1431-1438.
- [64] Sugiyama, E., Guerrini, M. M., Honda, K., Hattori, Y., Abe, M., Källback, P., ... & Sugiura, Y. (2019). Detection of a high-turnover serotonin circuit in the mouse brain using mass spectrometry imaging. *Science*, *20*, 359-372.
- [65] Shariatgorji, M., Nilsson, A., Fridjonsdottir, E., Vallianatou, T., Källback, P., Katan, L., ... & Andrén, P. E., *Nature methods* **2019**, *16*(10), 1021-1028
- [66] Matsuyama, R., Okada, Y., & Shimma, S., *Analytical and Bioanalytical Chemistry* **2022**, *414*(12), 3709-3718.
- [67] Merdas, M., Lagarrigue, M., Vanbellingen, Q., Umbdenstock, T., Da Violante, G., & Pineau, C., *Journal of Mass Spectrometry* **2021**, *56*(10), e4731.
- [68] Shariatgorji, M., Nilsson, A., Goodwin, R. J., Källback, P., Schintu, N., Zhang, X., ... & Andren, P. E., *Neuron* **2014**, *84*(4), 697-707.
- [69] Zhu, T., Wang, L., Tian, F., Zhao, X., Pu, X. P., Sun, G. B., & Sun, X. B., *Biomedicine & pharmacotherapy* **2020**, *129*, 110470.
- [70] He, H., Qin, L., Zhang, Y., Han, M., Li, J., Liu, Y., ... & Wang, X., *Analytical chemistry* **2019**, *91*(4), 2634-2643.
- [71] Hansen, R. L., Dueñas, M. E., & Lee, Y. J. *Journal of the American Society for Mass Spectrometry* **2018**, *30*(2), 299-308.
- [72] Yagnik, G. B., Hansen, R. L., Korte, A. R., Reichert, M. D., Vela, J., & Lee, Y. J. *Analytical chemistry* **2016**, *88*(18), 8926-8930.
- [73] Chiang, Cheng-Kang, Wen-Tsen Chen, and Huan-Tsung Chang. *Chemical Society Reviews* **40.3** **2011**, 1269-1281.

- [74] Yang, E., Fournelle, F., & Chaurand, P. *Journal of mass spectrometry*, **2020**, 55(4), e4428.
- [75] Havrilla CM, Hachey DL, Porter NA., *J Am Chem Soc.* **2000**, 122(33):8042-8055.

**Chapter 2. Optimization of ZnO Nanoparticles for the Detection and Imaging of Small Molecules in Rodent Brain Tissue Using Matrix-Assisted Laser/Desorption Ionization Mass Spectrometry**

## 2.1 Introduction

In MALDI MSI, imaging and detecting small molecules, those with  $m/z$  values below 1000 Da, gives significant challenges due to the interference from background signals of many matrix molecules. This challenge becomes especially prominent for molecules below 500 Da, which includes crucial neurotransmitters like glutamate, GABA, dopamine, and acetylcholine. As a solution, nanomaterials have emerged as an attractive alternative, offering many desirable characteristics such as a clean background signal, UV light absorption, a relatively high surface area, and the ability to detect various small molecules and neurotransmitters [1,2]. In particular, metal oxide nanoparticles have demonstrated the potential to detect these molecules while providing minimal background signal.

Despite the numerous advantages of metal oxide nanoparticles, their utilization remains limited due to inconsistencies in quality and size, along with a general lack of familiarity with how to handle them in the MALDI field. A study by Lee *et al.* conducted two large-scale nanoparticle screenings for small molecule analysis with MALDI MS, leading them to conclude that ZnO yielded weaker signals compared to other metal oxide NPs such as TiO<sub>2</sub>, and metal NPs such as Au and Ag [3,4]. They speculate that this might be attributed to ZnO's relatively low heat conductivity compared to other materials. However, recent work by the Yeung lab has shown that commercially available zinc oxide nanoparticles (ZnO NP) can perform as effectively as other metal oxide nanoparticles in imaging small molecules in biological tissue [5]. In positive ion mode, neurochemicals were found in the brain as adducts of sodium and potassium [5]. It is believed that the difference between Lee's work and Yeung's work arises from endogenous salt ions presented in biological tissue, aiding in ionization and the formation of cationic adducts for MALDI detection, which are not present in purified standards used in Lee's work [5]. Other factors like differences in shape, crystalline structure, and potential surface modifications may also impact the quality of analyte detection.

ZnO NP is pneumatically sprayed directly onto the tissue and mounted on the sample plate using the HTX TM sprayer. This spraying process generates a fine nanoparticle coating that facilitates desorption and provides signals for different small molecules such as GABA, glutamate, and glutamine [3]. In theory, the deposition of the NP onto the tissue should be highly consistent and controlled by the flow rate and number of spray passes. A significant challenge arises from the variation in quality and size of batch-to-batch dispersions commonly found in commercially available ZnO NP, leading to clogging of the inner filter in the sprayer, resulting in varying quality of detection and images obtained with this matrix.

To address this inconsistency in ZnO NP, a practical solution is proposed, along with a protocol to optimize this novel matrix for obtaining the highest-quality data. Finally, in the next chapter, the application of the optimized ZnO NP matrix is demonstrated, assessing the levels of different small molecules in rat brain tissue. This serves as a testament to the reliability and quality of ZnO NPs as a matrix for addressing biological questions, reinforcing its potential as a valuable tool in advancing the understanding of various complex biological systems.

## 2.2 Methodology and Materials

### 2.2.1 Chemicals and Supplies

GABA standards, ZnO NPs aqueous dispersion (20%, wt) with particle size  $\geq 100$  nm (product no. 721077), and Nonsterile Syringe Filters with a pore size of 1.2  $\mu\text{m}$  (part no. ISO-P2U192) were bought from Delta Scientific Laboratory Products (Mississauga, ON, Canada). ZnO NPs aqueous dispersions were bought in November 2016, March 2022, June 2022, and September 2022. Acetonitrile (ACN) was purchased from VMR (Karlsruhe, Germany), and EtOH was purchased from Commercial Alcohols (Toronto, ON, Canada). 4-(anthracene-9-yl)-2-fluoro-1-methylpyridin-1-ium iodide (FMP-10) was purchased from Tag-ON (Uppsala, Sweden), Trifluoroacetic acid (TFA) was purchased from Fisher Scientific (Waltham, MA, USA). ITO-coated glass slides were purchased from Hudson Surface Technology (Old Tapan, NJ, USA).

### 2.2.2 Matrix Solution Filtering and Preparation

ZnO NP bottle was sonicated for 30 seconds before preparing dispersions. Dispersions of ZnO NP were prepared in ACN/H<sub>2</sub>O (50/50% vol) at a concentration of 10 mg/mL. The dispersion was then sonicated for 10 minutes. Afterwards, 1 mL of the prepared solution was passed through the 1.2  $\mu\text{m}$  filter. The syringe-based filter was washed with 1 mL of ACN/H<sub>2</sub>O (50/50% vol) before usage. After filtering, the solution was diluted to 1 mg/mL and sonicated for another 5 minutes. GABA solutions were prepared in ACN/H<sub>2</sub>O (50/50% vol) at a concentration of 0.2 mg/mL for spotting experiments.

### 2.2.3 DLS Size Determination of Filtered Nanoparticle Dispersions

ZnO dispersions were diluted at 0.1 mL/mg for size distribution measurements using Dynamic Light Scattering (DLS). DLS measurements were performed with a Malvern Instruments Nano ZetaSizer with a 632.6 nm He-Ne laser. The scattered light was collected by a photodetector at a fixed scattering light angle. Before measurement, 1 mL of the dispersion was transferred to a clear disposable capillary cell, and its temperature was stabilized to 25 °C. Subsequently, the sample was allowed to stabilize for 120 seconds, during which the software optimized the measurement parameters for each sample. Three consecutive measurements, each consisting of 12-14 runs, were performed for every sample. The scattered light was then processed in a correlator, accumulating the intensity via an autocorrelation function. The correlation yielded an intensity size distribution, z-average diameter, and a ZnO NP dispersion polydispersity index (PDI).

### 2.2.4 UV-Vis Concentration Determination of Filtered Nanoparticle Dispersions

UV-Vis was used to determine the concentration of ZnO NP dispersions. UV-Vis absorbance measurements were performed under a DeNovix DS-11 Spectrophotometer using the microvolume measurement operating mode. After ensuring the sample surfaces were clean, the instrument was blanked using H<sub>2</sub>O by pipetting 1 µL onto the lower sample surface. The blank was then removed using a clean Kimwipe. Subsequently, ZnO dispersions at concentrations ranging from 2 mg/mL to 2 ng/mL were measured at 350 nm to form a calibration curve in Excel. The sample surface was cleaned using EtOH and a dry Kimwipe between every measurement. After constructing a calibration curve with the unfiltered samples, filtered ZnO dispersions with a pre-filtration concentration of 0.125 mg/mL were measured at 350 nm using the same method. The concentration of the filtered samples was determined using the Lambert-Beer equation with the assistance of the equation derived from the calibration curve.



### 2.2.5 Rodent Tissue Sectioning and Preparation

Cryostat sectioning of rat brain tissue was done at a thickness of 12  $\mu\text{m}$  under a temperature of -20  $^{\circ}\text{C}$  in a CM 1859 Cryostat. The brain tissue sections were thaw-mounted onto a stainless-steel plate at -80  $^{\circ}\text{C}$ . Before matrix deposition, the steel plates were dried in a desiccator under vacuum for 45 minutes at room temperature.

### 2.2.6 Matrix Deposition

The filtered ZnO NP dispersion was applied onto the stainless-steel plate using a pneumatic TM-Sprayer. The preferred spraying conditions were as follows: 1.0 mg/mL of ZnO NP in ACN/H<sub>2</sub>O (50/50%, vol), nozzle temperature of 65  $^{\circ}\text{C}$ , flow rate of 0.05 mL/min, nozzle moving velocity of 1200 mm/min, 4-36 passes, 3 mm line spacing, and pressure of 10 psi. For FMP-10, the conditions were as follows: 1.2 mg/mL of FMP-10 dispersion in ACN/H<sub>2</sub>O (70/30%, vol), nozzle temperature of 82  $^{\circ}\text{C}$ , flow rate of 1.7 mL/min, nozzle moving velocity of 1100 mm/min, 30 passes, 2 mm line spacing, and pressure of 6 psi. Upon completing the spraying cycle, the sprayer underwent a cleaning process. This process involved flushing the loop with a cleaning solvent of MeOH/ H<sub>2</sub>O/ TFA (50/50/ 0.1 %, vol) for 15 minutes. All FMP-10 runs and optimization were done by Mathusha Pusparajah.

### 2.2.7 MALDI MS Analysis and Data Processing

A Sciex 5800 MALDI TOF/TOF mass spectrometer (Framingham, MA, USA) with a 349 nm Nd laser with a pulse rate of 400 Hz was used for all MALDI imaging. Before each run, the laser energy and other parameters were manually optimized to obtain the highest signals for GABA and other target analytes. 0.75  $\mu\text{L}$  of a prepared 3 mg/ mL CHCA solution was spotted near the tissue to calibrate the masses. Spotting data was acquired using the Sciex TOF-TOF Series Explorer and Data Explorer software. Imaging was acquired using the Sciex TOF-TOF imaging software. Images were acquired at a raster size of 70  $\mu\text{m}$  for rat brains and 50  $\mu\text{m}$  for mouse brains.

## 2.3 Results and Discussion

### 2.3.1 DLS Analysis of Particle Size Before and After Filtration of the ZnO NP Dispersion

The average size distribution of the four commercially purchased ZnO NP dispersions was 282.76 nm. The primary size of the different dispersions ranged from 230 to 300 nm. These sizes surpass their intended particle size provided by the distributors by more than three times. This phenomenon has been extensively reported for metal oxides, particularly when the nanoparticles are in a water-based medium [5-9]. More importantly, the DLS analysis indicates the presence of a cluster peak of aggregates at around 5000 nm. This poses a problem, given that the inlet diameter of the TM-Sprayer is only 2000 nm. The DLS size distribution of the latest batch is shown in **Figure 2.1**. As a result, it's possible to explain the inconsistencies in spraying and the recurring issue of dispersion clogging by these aggregates.

A new DLS analysis was conducted on the suspension after passing it through the 1.2  $\mu\text{m}$  filter. The updated size distribution shows the removal of the aggregates at 5000 nm, as shown in **Figure 2.1**. The primary particle size appears largely unaffected, and the minor differences between filtered and unfiltered samples can be attributed to the fact that the measurements were taken from different samples of the same batch. With the DLS analysis, it is possible to conclude that the syringe filter successfully separates the larger aggregates from the sample, potentially rendering them compatible with the automatic sprayer.

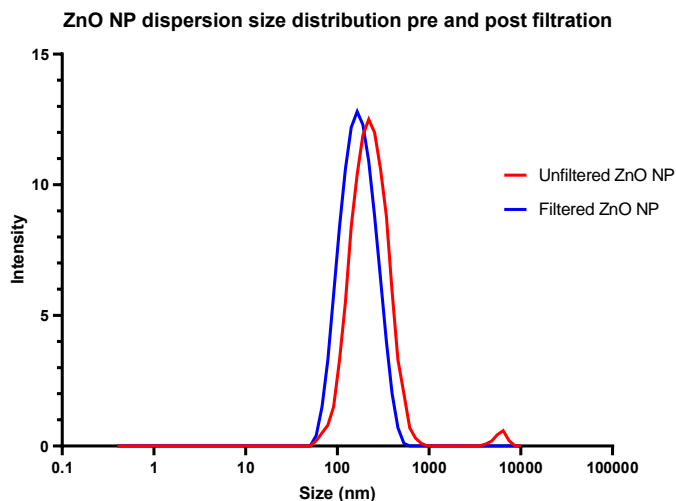


**Figure 2.1.** DLS size distribution before filtration (red) and after filtration (blue) for the batch bought in September 2022

### 2.3.2 Concentration Analysis of Filtered ZnO Dispersion

To assess the percentage of recovered ZnO from the filtered dispersions, a UV-calibration curve was constructed using the unfiltered NPs at various dilutions at 350 nm. The initial concentration was determined by weighing 100  $\mu\text{L}$  of the ZnO suspension and allowing it to dry under ambient conditions for 5 days, after which it was weighed again. The concentration obtained agreed with the value given by the provider (20% wt). Both the entire batch (bottle) and each dilution were sonicated to ensure the uniform distribution of nanoparticles in each sample. This step was taken to homogenize the samples as larger particles tend to settle at the bottom, leading to a heterogeneous dispersion as shown in **Figure 2.2**.

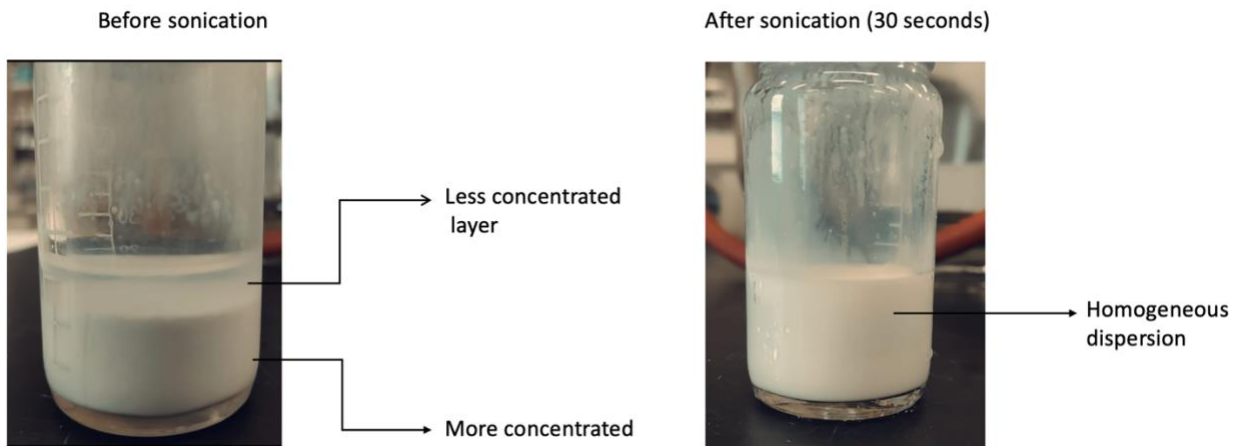


**Figure 2.2.** ZnO NP dispersion before (left) and after (right) sonication. The heterogeneous concentration before sonicating can be explained by the bigger nanoparticles sinking to the bottom.

The resultant equation of the calibration curve of the unfiltered ZnO dispersion was  $17.391x + 0.2063$  with an  $R^2$  value of 0.999. Following the construction of the calibration curve, five filtered samples were measured using the UV-Vis Spectrometer. This was carried out to assess the material loss due to filtration and the reproducibility of the filters. The UV-Vis Spectroscopy revealed that the filtration resulted in an average recovery of 92% demonstrating high reproducibility with a relative standard deviation (RSD) of 6%. As previously mentioned, sonication is a crucial step to maintain the even dispersion of the nanoparticles, as they tend to settle if left undisturbed. To further support this theory, a single sample was placed in a vial and allowed to settle for 3 hours. UV-Vis samples were periodically taken from the surface to monitor the drop in concentration. A significant decrease in NP dispersion concentration was observed after 45 minutes, as illustrated in **Figure 2.4**.

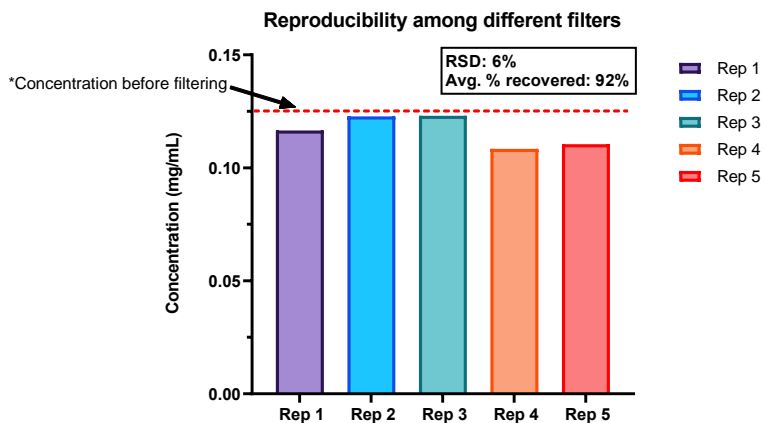


**Figure 2.3.** Reproducibility of concentration after filtration of the ZnO NP dispersion

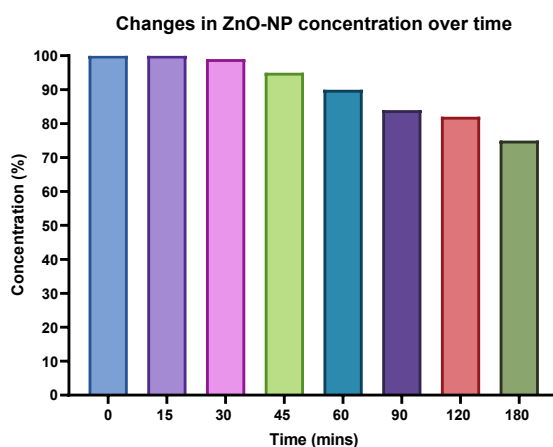


**Figure 2.4.** Concentration of ZnO NP dispersion dropped over time due to the gradual settling of NP

### 2.3.3 Optimization of Matrix Deposition on Rodent Brain Tissue for Small Molecule Detection

#### 2.3.3.1 ZnO Nanoparticle Spotting on Standards Analysis

Before applying the filtered matrix to tissue samples, comprehensive spotting experiments were conducted to assess the suitability of the filtered matrix and fine-tune its performance for the detection of small molecules. GABA standards were prepared at a concentration of 0.2 mg/mL, and they were mixed with NP suspension at varying concentrations to evaluate the potential introduction of leached chemicals that could compromise the sample integrity. After analyzing and comparing the results, an optimal concentration of 1 mg/mL was determined for the filtered NP suspension. The mass spectrum of the GABA standard at this optimal matrix concentration is depicted in **Figure 2.5**.

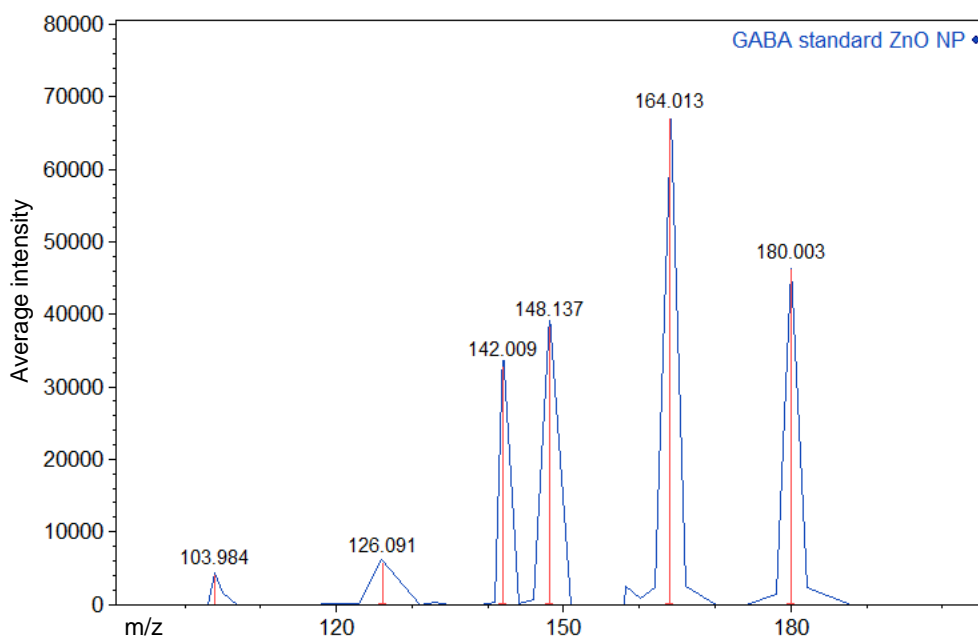


**Figure 2.5.** Positive ion mass spectrum of a 0.2 mg/mL GABA standard: 103.984  $m/z$   $[M + H]^+$ ; 126.091  $m/z$ ,  $[M + Na]^+$ ; 142.009  $m/z$ ,  $[M + K]^+$ ; 148.137  $m/z$ ,  $[M + 2Na-H]^+$ ;  $m/z$  164.013  $m/z$   $[M - H + Na + K]^+$ ; 180.003  $m/z$   $[M - H + 2K]^+$  with 5 mg/mL filtered ZnO matrix solution.

The results align well with the existing literature confirming that the ZnO NP matrix provides a clean MS background with no matrix peaks in the low mass range region. Furthermore, the 1.2  $\mu\text{m}$  size filter showed no significant signal contamination. The mass spectra were acquired in positive mode, as it exhibited a significantly superior signal than the negative mode. Notably, all GABA adducts, especially  $[\text{M} + \text{Na}]^+$  and  $[\text{M} + \text{K}]^+$  are strong and have a high signal-to-noise ratio as opposed to the protonated GABA ion  $[\text{M} + \text{H}]^+$ . Although this phenomenon is not commonly observed in traditional matrices, it has been established that the detection of the ion as  $\text{Na}^+$  and  $\text{K}^+$  adducts is not a limiting factor in the detection of these analytes [4, 10].

#### 2.3.3.2 Matrix Deposition Parameters Optimization

As mentioned in the previous chapter, the quantity of matrix deposited onto the tissue plays a crucial role in shaping the quality and intensity of analyte signals. The optimal spray amount of ZnO NPs was determined, focusing on GABA and Glutamate signals in positive mode in wild-type rat coronal brain tissue sections, given their fundamental significance as analytes in various brain functions. As previously stated, these analytes are predominantly present in their potassium adducts. Other molecules were also found using the matrix, including several fatty acids and amino acids. To optimize the amount of matrix sprayed onto the tissue, a range of eight different number of passes settings, spanning from 4 to 32 were tested to achieve the most efficient deposition. The nucleus accumbens (NAc) core was the selected brain region for quantifying peak intensities. This region was chosen as most neurotransmitters are very region-specific and the NAc is known to contain plenty of GABA. The intensity plot shows that the signal intensity for both analytes reaches their maximum point at 20 passes, where they start to decrease after as noted in **Figure 2.6**. It can be speculated that the ZnO NP matrix layer is too thick, and the laser does not fully reach the analytes at this point.

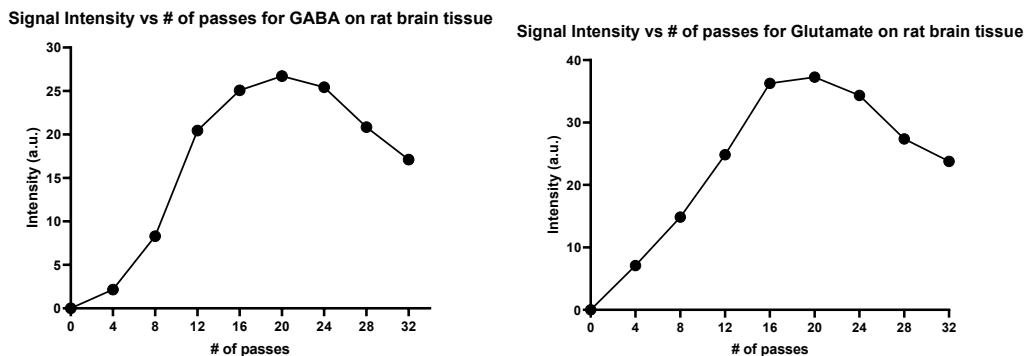


**Figure 2.6.** The peak intensities of (A) GABA and (B) glutamate determined from the nucleus accumbens core region of rat brain tissue after different numbers of NP spraying passes.

In the 20-24 passes range, the image quality is very high, providing good spatial resolution with differentiating changes in analyte types and concentration in the brain. GABA is mainly detected in the NAc while Glutamate is more widespread through the brain. This is by previous studies and confirms that the detected signals correspond to the target analytes [4]. Other interesting molecules include Cholesterol and Glutamine, which are two analytes essential for the well-functioning of the brain. GABA, Glutamate, and Cholesterol can be observed in **Figure 2.7**.

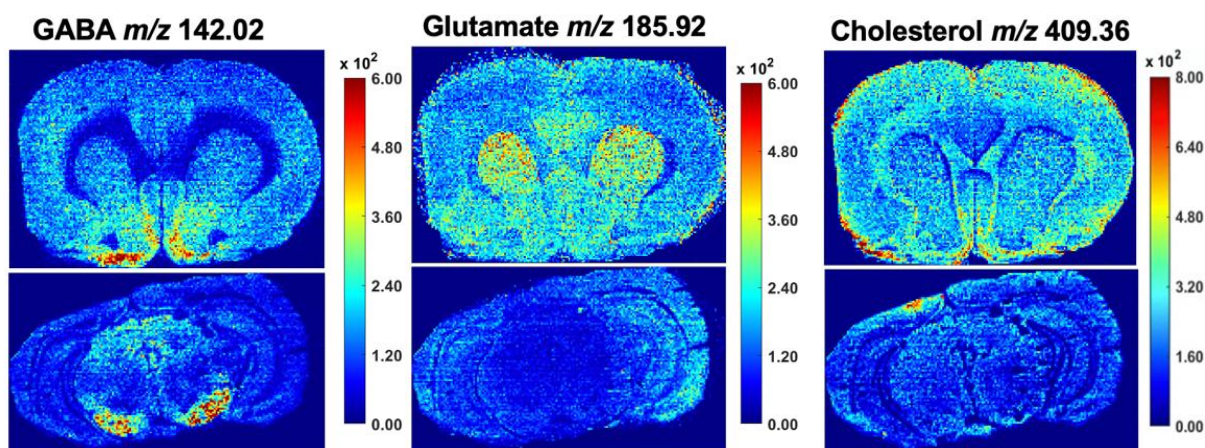


**Figure 2.7.** MSI spatial distribution in positive mode of GABA (left), Glutamate (center), and Cholesterol (right) at Bregma  $-6.00$  mm and Bregma  $2.52$  mm, respectively at 20 passes with a raster size of  $70 \mu\text{m}$ .



## 2.4 Comparison Between Optimized ZnO NP and Other Matrices for the Detection of Small Molecules

The detection of cholesterol was a welcome surprise. Chaurand *et al.* recently developed a silver-assisted laser desorption ionization (AgLDI) MS approach for the imaging of cholesterol from thin tissue sections with high specificity and sensitivity. Their AgLDI methodology is regarded as the best imaging data for cholesterol [11-13]. Furthermore, their quantification work with cholesterol has shown consistent results, especially in rat brains [15]. While the initial intention was not to sense cholesterol with the optimized ZnO NP matrix, comparing the obtained results with those reported in the literature [11-14] provides a valuable assessment of the sensitivity and flexibility of the ZnO NP matrix. The results appear highly promising, with cholesterol being detected throughout the entire brain, showing a higher abundance in the white matter. **Figure 2.7** illustrates a similar detection pattern, particularly noticeable at Bregma 2.52 mm. Interestingly, cholesterol is detected as potassiated and sodiated adducts with the ZnO NP matrix, whereas with AgLDI, it is detected as silver adducts. The reason for this difference remains unknown; no zinc adducts were found for cholesterol or any other molecules. It can be speculated that zinc does not ionize the molecule strongly enough to reach the detector, resulting in it staying within the tissue.

To compare the signal intensity and the molecules detected, MALDI runs with FMP-10 were conducted alongside ZnO NP for the remaining small molecules. FMP-10 has gained wide recognition as an effective matrix for the ionization of GABA, serotonin, dopamine, and other neurotransmitters [16]. Coronal adjacent rat brain tissue sections were run for both matrices. In our experiments, ZnO NP detected twelve small molecules, while FMP-10 detected fifteen. Notably, FMP-10 exhibited generally higher intensity signals as depicted in **Figure 2.8**, although with less defined features. The ionization method of FMP-10 is exceptionally potent, though its reliability may be subjected to certain challenges. While several calibration curves have demonstrated the reliability of FMP-10 OTCD in fully ionizing standards on tissue [17], factors such as instrument sensitivity, temperature, and reaction time of the matrix, among others, may introduce challenges in accurate quantification with FMP-10. Conversely, the ZnO NP matrix does

not rely on OTCD, making it more dependable for relative quantitation across different tissues, despite yielding lower signal intensities.

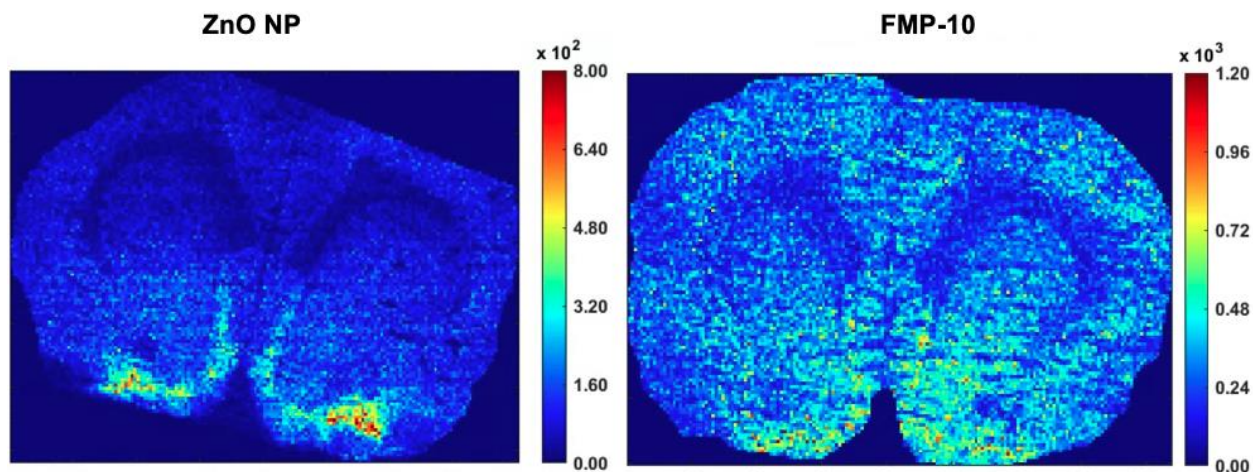


**Figure 2.8.** GABA molecule detected with ZnO NP as a matrix (left) and FMP-10 (right).  
The FMP-10 signal is higher but has less defined spatial features.

Additionally, ZnO NP possesses the capability to ionize molecules that lack phenolic hydroxyl and primary or secondary amine groups. This broader range means that molecules like fatty acids can be observed using ZnO NP, which differs from FMP-10, which can only detect specific neurotransmitters and amino acids containing these functional groups. The most noteworthy molecule detected by ZnO NP, which isn't detected by FMP-10, is glutamate. Not only is it detected with relatively high intensity and excellent spatial distribution, but it is also a critical amino acid highly relevant to numerous neurochemical processes. Another interesting molecule identified by ZnO NP is glutamine, which works closely with glutamate and is also not detected by FMP-10. These findings, along with the detection of three fatty acids, give the optimized ZnO NP matrix a distinct advantage over FMP-10 for neurochemical applications. Importantly, FMP-10 cannot detect cholesterol, whereas ZnO NP has demonstrated its effectiveness in cholesterol detection, as shown earlier. While it is not possible to definitively state that ZnO NP is superior to FMP-10, it indeed has an advantage in the detection of certain molecules, such as glutamate and glutamine. Furthermore, the background signal from ZnO NP is cleaner, particularly in the 250-

450  $m/z$  range. FMP-10 exhibits strong peaks, making it less flexible and limiting its potential as a matrix. A comparison of both spectra can be observed in **Figure 2.9**. All detected molecules for the ZnO NP matrix are seen as well.

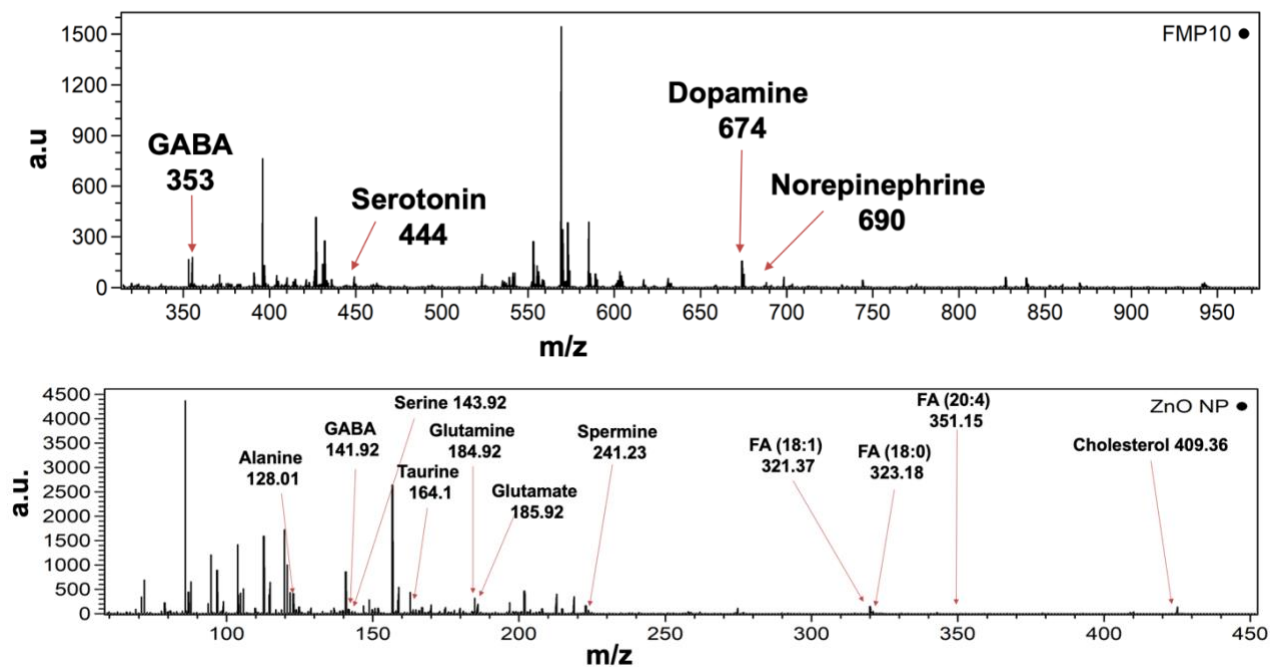


**Figure 2.9.** Average mass spectra in positive ion mode of the nucleus accumbens core region of the rat brain for FMP-10 (top). Average mass spectrum in positive ion mode of the nucleus accumbens core region of a rat brain for ZnO NP (bottom)

## 2.5 Conclusion

Commercially available ZnO NP dispersion was optimized to serve as a MALDI matrix for the detection of small molecules. This matrix exhibits numerous characteristics including a low background signal in the low mass range, excellent detection capabilities for small molecules, high sensitivity, and a relatively high surface area. Using 1.2  $\mu\text{m}$  size filters, the matrix was successfully filtered, removing aggregates measuring successfully removed aggregates measuring  $> 5000$  nm. These aggregates, which had previously caused clogging and reproducibility issues, were effectively separated, resulting in consistent reproducibility of recovered ZnO and maintaining the matrix's ability to provide high spatial-resolution images.

The filtered ZnO NPs matrix was specifically optimized for the detection of small molecules, GABA, and Glutamate. These molecules were consistently detected in coronal sections of rat brain tissue, showing good spatial resolution and strong signals. In comparison to the more established FMP-10 matrix, the optimized ZnO NP matrix exhibits the ability to detect several unique analytes, most notably Glutamate, Glutamine, fatty acids, and Cholesterol.

Although the signal intensity of the ZnO NP matrix may not match that of FMP-10, its advantage lies in the absence of OTCD dependency. This means that the signals obtained with the ZnO NP matrix are more reliable for relative quantification, as they are not influenced by external factors like temperature and reaction time. While ZnO's performance may not be strictly superior, it presents itself as an interesting alternative capable of detecting several essential molecules, providing reproducible imaging data within a reliable automated workflow routine for a wide range of samples.

## 2.6 References

- [1] Yang, E., et al., *Journal of Mass Spectrometry* **2019**, 55(4), e4428.
- [2] McLaughlin, N. et al., *J. Am. Soc. Mass Spectrom.* **2020**, 31(12), 2452-2461.
- [2] Yagnik, G. B., Hansen, R. L., Korte, A. R., Reichert, M. D., Vela, J., & Lee, Y. J. *Analytical chemistry*. **2016**, 88(18), 8926-8930.
- [3] Hansen, R. L., Dueñas, M. E., & Lee, Y. J., *Journal of the American Society for Mass Spectrometry*. **2018**, 30(2), 299-308.
- [4] Chen, Chaochao, et al. *Journal of the American Society for Mass Spectrometry* **2021**, 32.4.1065-1079.
- [5] Fatehah, Mohd Omar, Hamidi Abdul Aziz, and Serge Stoll. *Journal of Colloid Science and Biotechnology* **2014**, 3.1. 75-84.
- [6] Chung, S. J., et al. *Powder Technology* **2009**,194.1-2. 75-80.
- [7] Hakim, Luis F., et al. *Powder Technology* **2005**, 160.3. 149-160.
- [8] Zhang, Yang, et al. *Water Research* **2008**, 42.8-9. 2204-2212.
- [9] Zhou, Dongxu, Samuel W. Bennett, and Arturo A. Keller. *PloS one* **2012**, 7.5. e37363.
- [10] Truong, J. X., Spotbeen, X., White, J., Swinnen, J. V., Butler, L. M., Snel, M. F., & Trim, P. J., *Analytical and Bioanalytical Chemistry* **2021**, 413, 2695-2708.
- [11] Yang, E., Fournelle, F., & Chaurand, P., *Journal of mass spectrometry* **2020**, 55(4), e4428.
- [12] Dufresne M, Patterson NH, Lauzon N, Chaurand P., *Adv Cancer Res* **2017**, 134:67–84.
- [13] Yang E, Fournelle F, Chaurand P. *J Mass Spectrom.* **2021**;55(4).
- [14] Lauzon N, Dufresne M, Beaudoin A, Chaurand P. *Journal of Mass Spectrometry* **2017**, 52(6):397–404.
- [15] Nezhad, Z. S., Salazar, J. P., Pryce, R. S., Munter, L. M., & Chaurand, P., *Analytical and Bioanalytical Chemistry* **2022**, 414(23), 6947-6954.
- [16] Shariatgorji, M., Nilsson, A., Fridjonsdottir, E., Vallianatou, T., Källback, P., Katan, L., ... & Andrén, P. E. *Nature Methods* **2019**, 16(10), 1021-1028.
- [17] Shariatgorji, R., Nilsson, A., Strittmatter, N., Vallianatou, T., Zhang, X., Svenningsson, P., ... & Andrén, P. E., *Journal of the American society for mass spectrometry* **2020**, 31(12), 2553-2557.

**Chapter 3. Relative Quantitation of Neurotransmitters and Other Small Molecules in Brains from Adolescent Rats Subjected to Edible Delta-9-Tetrahydrocannabinol (THC) Consumption Using Optimized ZnO Nanoparticles by Matrix-Assisted Laser/Desorption Ionization Mass Spectrometry.**

### 3.1 Introduction

Cannabis usage has surged in Canada, particularly in young users. The recent legalization of cannabis has inadvertently diminished the perception of its inherent health risks with regular use [1]. However, various studies indicate that consistent cannabis use during developmental stages increases the risk of various psychiatric conditions [2-3]. Furthermore, the primary component of cannabis,  $\Delta^9$ -tetrahydrocannabinol (THC), has witnessed a significant rise in usage. THC use among adolescent users has been linked to adverse long-term effects on decision-making and impulse control [4]. Consequently, understanding the detrimental effects of THC, particularly during critical cognitive development, is of high importance.

Cannabis edibles are food products infused with cannabis extract [5-6]. They take various forms such as gummies, chocolates, and baked goods. Edibles have gained popularity for cannabis consumption, especially recreationally. For instance, in the United States, a national survey revealed that 29.8% of respondents who had used cannabis reported consuming it in edible form [5]. Like other modes of cannabis consumption, edibles also carry inherent risks. Consumption of edible THC has led to episodes of severe cannabis-induced behavioral impairment. However, in healthy adult users, these psychotic symptoms are short-lived and last only during the period of intoxication [6]. Nonetheless, literature on such cases, particularly involving edibles, remains limited.

The Laviolette lab at Western University has previously studied the effects of THC on normal brain development using different animal models with the help of MALDI MSI [7-8]. Evidence from Laviolette's work suggests that the long-term behavioral impact of THC exposure during adolescence can be attributed to disruptions in the mesocorticolimbic circuits, specifically the prefrontal cortex (PFC) and nucleus accumbens (NAc) [8]. These brain regions are integral to the reward system and are among the last areas to mature [9]. The neural connections between the PFC and NAc are established by GABAergic and glutamatergic neurons within the central nervous system.

The proper functioning of the central nervous system is partially upheld by the glutamate-glutamine cycle, a biochemical process occurring between neurons and astrocytes (supporting cells in the brain). In this process, neurons release glutamate, an excitatory neurotransmitter between nerve cells. The excess glutamate released is absorbed by astrocytes and converted into glutamine through the enzyme glutamine synthetase. This glutamine is transported back to neurons from astrocytes, where it is reconverted into glutamate, restarting the cycle [10]. With THC exposure during adolescent brain development, the neurotransmitter systems in the central nervous system are disrupted due to the activation of cannabinoid type 1 receptors (CB1Rs). These CB1Rs activate GABAergic and glutamatergic neurons, leading to alterations in neurotransmitter levels in the NAc and PFC regions [11].

MALDI MSI offers molecule identification, relative quantitation, and molecule distribution in tissue samples, encompassing a wide array of biomolecules pertinent to various neurotransmission processes, including the glutamate-glutamine cycle. Furthermore, the previously developed and optimized ZnO NP matrix has demonstrated its effectiveness in detecting and mapping GABA, Glutamate, and Glutamine in rat brain tissue. The superior spatial resolution achieved with this matrix facilitates the examination of overall neurotransmitter levels in different regions, thus aiding in the study of adolescent rat brains exposed to chronic edible THC consumption. These findings can contribute to a better understanding of the short- and long-term effects of edible THC consumption during adolescence, particularly in the NAc subregions of the core and shell. Lastly, employing FMP-10, we can evaluate the reliability of the ZnO NP matrix in accurately quantifying and detecting GABA, highlighting the matrix's potential in long-term biological studies.



## 3.2 Experimental Section

### 3.2.1 Chemicals and Supplies

ZnO NP aqueous dispersion (20%, wt) with particle size  $\geq 100$  nm (product no. 721077), Nonsterile Syringe Filters with a pore size of 1.2  $\mu\text{m}$  (part no. ISO-P2U192) were bought from Delta Scientific Laboratory Products (Mississauga, ON, Canada). ACN was purchased from VMR (Karlsruhe, Germany). 4-(anthracene-9-yl)-2-fluoro-1-methylpyridin-1-ium iodide (FMP-10) was purchased from Tag-ON (Uppsala, Sweden) Trifluoroacetic acid (TFA) was purchased from Fisher Scientific (Waltham, MA, USA). Metal plates were purchased from Hudson Surface Technology (Old Tapan, NJ, USA). Male and female adolescent Sprague-Dawley rats were obtained on postnatal day (PND) 28 from Charles River Laboratories (Quebec, Canada). Cannabis-derived THC was purchased from Canopy Health Innovations Inc. (Toronto, Canada).

### 3.2.2 Animals and Housing

At arrival, adolescent Sprague-Dawley rats were pair-housed in controlled conditions (constant temperature, humidity, 12h light/dark cycle) with free access to food and water. All procedures and protocols were approved by the Canadian Council on Animal Care and the Animal Care Committee at Western University for the appropriate care and use of rats. All animal care was done by Dr. De Vuono from the Laviolette lab.

### 3.2.3 Drug Administration

The Cannabis-derived THC was mixed with hazelnut spread (Nutella) to create edibles. Nutella is very yearning for rats, so food restriction was not required before the appearance of edible samples. Rats were given edibles twice daily from PND 35 to 45 with escalating doses of THC. Control rats received the same edible schedule (volume adjusted per body weight) of vehicle (VEH; Nutella). Male and female rats were randomly assigned to THC or vehicle (VEH) conditions (male; n=5 THC, n=5 VEH; female; n=5 THC, n=5 VEH). To make sure that cage mates did not eat each

other's edibles, one cage mate went into their separate "feeding cage". After ingestion (around 20 minutes, rats returned to their original cages. The assigned cage mate was moved to counterbalance each day. All subjects were previously given 0.5 mL of Nutella twice a day for free days to habituate themselves with Nutella before drug administration. The total ingested amount of Nutella was 6 g/kg of body weight per edible. The dosing schedule of THC was 1 mg/kg; PND 35-37; 2.5 mg/kg; PND 38-41; 5 mg/kg; PND 42-45, resulting in THC edible concentrations of 0.167 mg/g, 0.417 mg/g, and 0.833 mg/g of Nutella, respectively. This workflow and concentrations were chosen to overcome the potential development of tolerance and taste avoidance of THC. Rats were sacrificed around PND 120 with an overdose of pentobarbital, brains extracted, and flash frozen on dry ice and stored at -80°C until ready for sectioning. All drug administration was done by Dr. De Vuono from the Laviolette lab.

### 3.2.4 Sample Preparation for MSI

Cryostat sectioning of rat brain tissue was done at a thickness of 12  $\mu\text{m}$  under a temperature of -20 °C in a CM 1859 Cryostat. The chosen section was around Bregma 2.11 mm where both PFC and NAc regions were visible. The brain tissue sections were thaw-mounted onto a stainless-steel plate at -80 °C. Before matrix deposition, the steel plates were dried in a desiccator under vacuum for 45 minutes at room temperature. On the same plate, 4 different tissues were mounted: Male Vehicle, Female Vehicle, Male THC-treated, and Female THC-treated.

Previously to matrix spraying, the commercially available ZnO NP was filtered by a 1.2-  $\mu\text{m}$  syringe filter. The filtered ZnO NP dispersion was deposited onto the stainless-steel plate using a pneumatic TM-Sprayer. The preferred spraying conditions were as follows: 1.0 mg/mL of ZnO NP in ACN/H<sub>2</sub>O (50/50%, vol), nozzle temperature of 65 °C, flow rate of 0.05 mL/min, nozzle moving velocity of 1200 mm/min, 20 passes, 3 mm line spacing and pressure of 10 psi. For FMP-10 the conditions were as follows: 1.2 mg/mL of FMP-10 dispersion in ACN/H<sub>2</sub>O (70/30%, vol), nozzle temperature of 82 °C, flow rate of 1.7 mL/min, nozzle moving velocity of 1100 mm/min, 30 passes, 2 mm line spacing and pressure of 6 psi. After completing the spraying cycle, the sprayer

underwent a cleaning process. This process involved flushing the loop with a cleaning solvent of MeOH/ H<sub>2</sub>O/ TFA (50/50/ 0.1 %, vol) for 15 minutes. All FMP-10 runs were done by Mathusha Pusparajah.

### 3.2.5 MALDI MS Data Processing and Analysis

A Sciex 5800 MALDI TOF/TOF mass spectrometer (Framingham, MA, USA) equipped with a 349 nm Nd laser operating at a pulse rate of 400 Hz was used for all MALDI imaging experiments. Before each run, laser energy and other parameters were manually optimized to obtain the highest intensities for GABA and other target analytes. To calibrate the masses, 0.75  $\mu$ L of a prepared 3 mg/ mL CHCA solution was spotted near the tissue. The imaging process was conducted using the Sciex TOF-TOF imaging software.

Imaging was performed at a raster size of 70  $\mu$ m for rat brains. For relative quantitation, mass spectra were generated by extracting the averaged  $m/z$  and intensity values from the defined regions of interest (ROI) NAc core and NAc shell. The peak areas corresponding to [GABA + K] at  $m/z$  141.92, [Glutamate + K] at  $m/z$  185.92, and [Glutamine + K] at  $m/z$  184.92 were integrated. Subsequently, the peak area ratios between the THC-treated and vehicle-treated rat brains were calculated using MATLAB.

Five replicates were measured for each sex and both hemispheres of each run were averaged to form a single data point. Subsequently, each side's data was normalized to the overall average signal intensity of that specific experiment. The mean, along with the associated standard deviation (SD) and standard error of the mean (SEM), was computed for each data point. Finally, a Students t-test was conducted to assess the statistical significance of the results. All figures and statistics were made using GraphPad.

### 3.3 Results and Discussion

#### 3.3.1 Identification of Small Molecules GABA, Glutamate, and Glutamine in the Rodent Brain Sections

The identifications of GABA, Glutamate, and Glutamine involved comparing their  $m/z$  values obtained from MALDI MSI within a list of theoretical values for these three molecules, considering the potassiated adduces, with a 50-ppm tolerance range. Additionally, the ion images from the three different molecules were compared to the existing ones in the literature. Notably, the ion distributions for GABA, Glutamate, and Glutamine were similar in both male and female brains subjected to both THC and VEH treatments. This consistency aligns with previous research indicating that THC exposure during adolescence does not significantly alter the spatial distributions of neurotransmitters in the Nucleus Accumbens (NAc) subregions [8].

The obtained images exhibited similar distributions to those shown in the previous chapter. GABA was predominantly observed in the NAc region, while Glutamate was prominently located in the grey matter region, encompassing the neuronal cell bodies that release neurotransmitters participating in the glutamate-glutamine cycle [12]. A similar pattern was observed for glutamine, with a more uniform distribution throughout the brain but notably absent from the black matter region. These observations are consistent with existing literature findings.

Finally, GABA ion distributions between both matrices, FMP-10 and ZnO NP were very similar, although the former showed less distinct features while displaying higher signal intensity, consistent with the findings from the previous chapter. A scheme of the regions can be found in **Figure 3.1**.

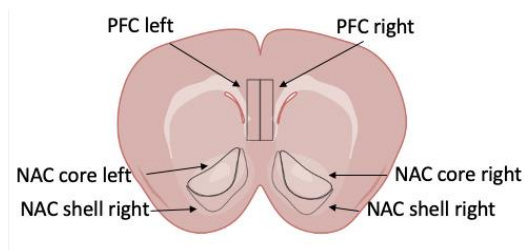


**Figure 3.1.** Schematic diagrams showing ROIs

### 3.3.2 Relative Quantitation of Small Molecules Glutamate, GABA, and Glutamine between sexes and THC-treated and Vehicle-treated Rat Brains.

As previously mentioned, the primary objective of this study was to compare the differences in neurotransmitter levels within the NAc subregions of adolescent rat brains, considering both sexes, following chronic consumption of edible THC compared to vehicle treatment. Recognizing the inherent variability that can arise in MALDI analyses, a strategy was employed to mitigate these potential discrepancies. To address this concern, one sample from each group (vehicle-treated and THC-treated) for both sexes was placed on the same plate. This allowed for the calculation of peak area ratios between the vehicle-treated and THC-treated groups for both sexes. This approach aided in normalizing the data and minimizing potential experimental variations. A total of 5 replicates were conducted, resulting in multiple peak area ratios for each of the three molecules within both the NAc core and shell regions.

Following chronic exposure to THC through edible consumption, a noticeable reduction was observed in the concentrations of all three molecules in both the NAc core and shell regions, regardless of sex. Specifically, for GABA, there was an approximate decrease of 30% and 25% in males and females, respectively, within the NAc core. In the NAc shell region, a reduction of around 32% was observed in both males and females. Importantly, these changes were statistically highly significant ( $p < 0.001/**$ ). Graphs depicting the GABA ratios for both sexes in both regions, utilizing the ZnO NP matrix, are presented in **Figure 3.2**.

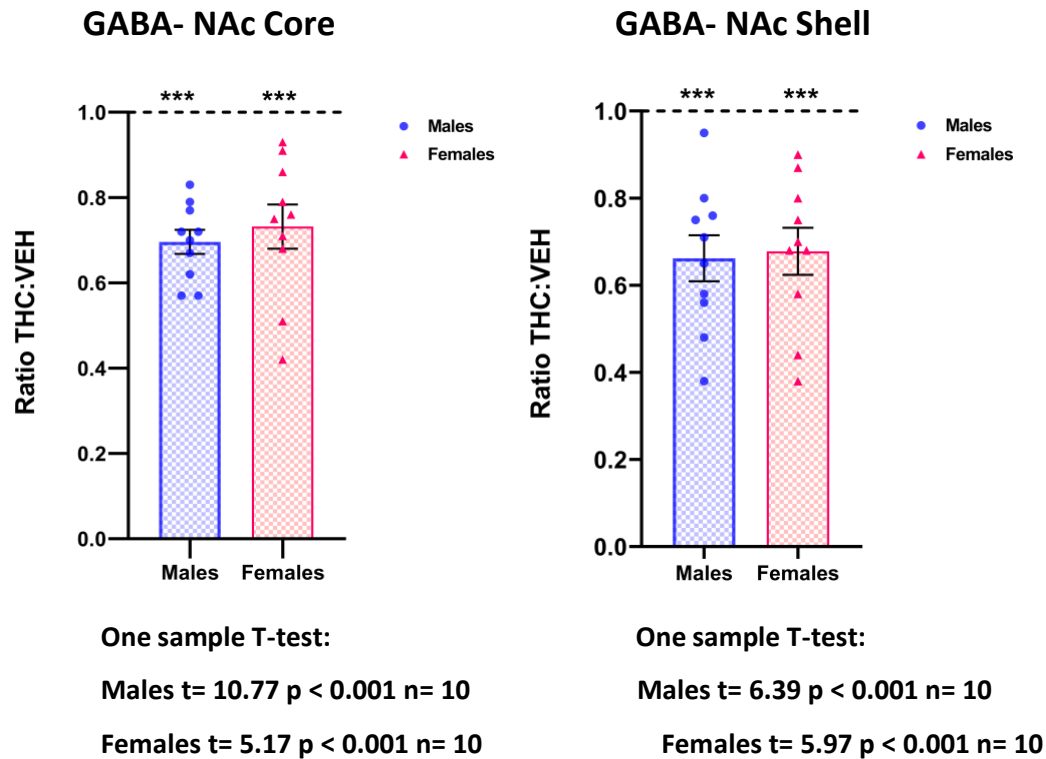
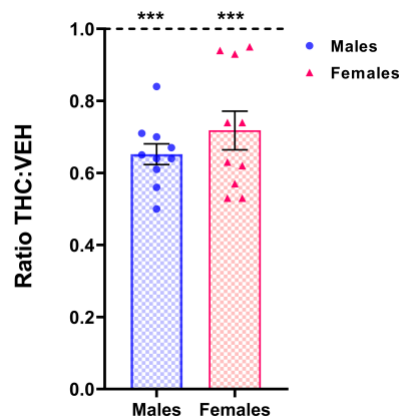


**Figure 3.2.** Peak area ratios of GABA between THC-treated and vehicle-treated adolescent rat brains in the NAc core (left) and shell (right) regions. Asterisks indicate that the featured ratio is statistically significant in the one sample T-test (\*\* $p < 0.001$ )

Conversely, Glutamate also reveals promising findings. Notably, there was a reduction of approximately 37% for males and 25% for females within the NAc core region. In the NAc shell, males exhibited a slightly lower decrease compared to their core counterparts, with an approximate reduction of 25%, whereas females showed a decrease of around 30%. As with GABA, all these changes proved to be highly statistically significant ( $p < 0.001$ ). This emphasizes the matrix's robustness in effectively identifying tissue changes. Visual representations of the Glutamate ratios for both sexes in both regions are illustrated in **Figure 3.3**.

### Glutamate NAc Core

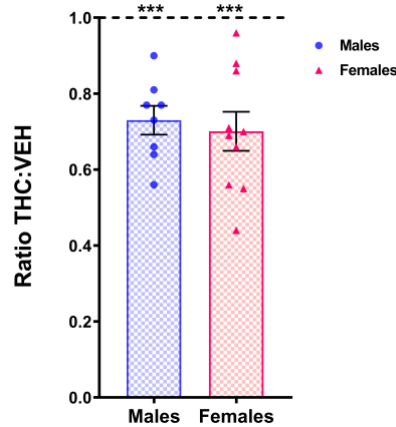


One sample T-test:

Males  $t = 12.06$   $p < 0.001$   $n = 10$

Females  $t = 5.26$   $p < 0.001$   $n = 10$

### Glutamate- NAc Shell



One sample T-test:

Males  $t = 7.00$   $p < 0.001$   $n = 10$

Females  $t = 5.82$   $p < 0.001$   $n = 10$

**Figure 3.3.** Peak area ratios of Glutamate between THC-treated and vehicle-treated adolescent rat brains in the NAc core (left) and shell (right) regions. Asterisks indicate that the featured ratio is statistically significant in the one sample T-test (\*\* $p < 0.001$ )

Lastly, Glutamine shares the trends observed in the other two molecules. Within the NAc core region, a reduction of approximately 25% for males and 35% for females was observed. Akin results were seen in the NAc shell region, with both males and females exhibiting decreases of around 30% and 35% respectively. Similarly, to GABA and glutamate, changes in both NAc regions were statistically highly significant. It's noteworthy that the decrease in these three molecules appears to be interconnected, potentially reflecting a cascade effect between them. A decrease in glutamate might lead to a subsequent decrease in glutamine through the glutamate-glutamine cycle, as explained earlier. Graphs of the Glutamine ratios can be seen in **Figure 3.4**.

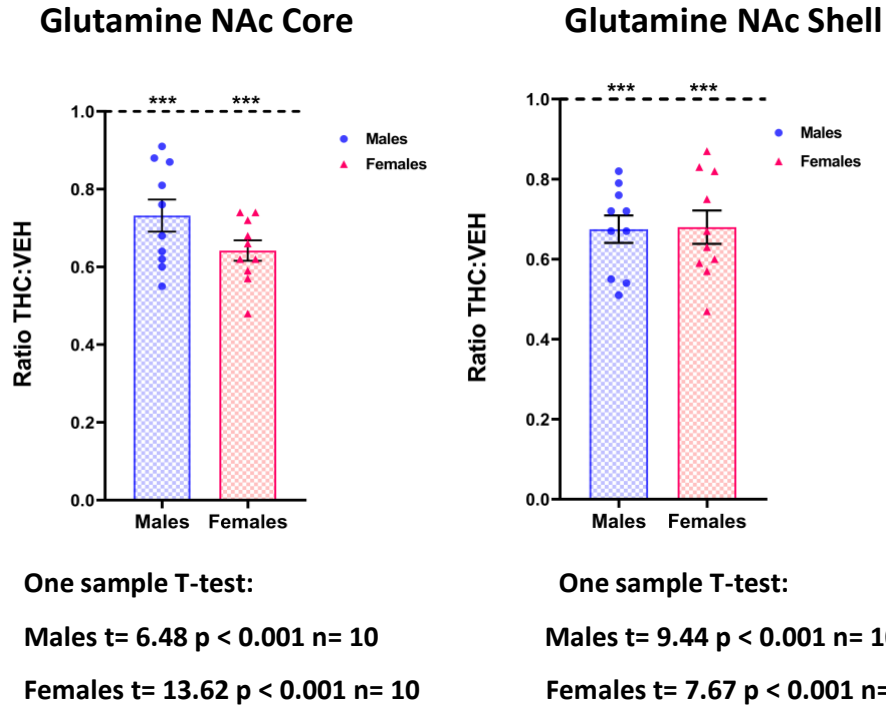


**Figure 3.4.** Peak area ratios of Glutamine between THC-treated and vehicle-treated adolescent rat brains in the NAc core (left) and shell (right) regions. Asterisks indicate that the featured ratio is statistically significant in the one sample T-test (\*\*\*)  $p < 0.001$

To further explain the interconnection between the three analytes, it is crucial to understand the Glutamine- Glutamate cycle and the Glutamate- GABA cycle. The former has already been explained in the introduction, but the latter is equally key to the correct function of the brain. Glutamate is converted into GABA through a special enzyme located in the brain called glutamic acid decarboxylase [13]. This enzyme converts the free glutamate in the brain into GABA by losing a carboxylic acid group in the form of  $\text{CO}_2$ . Once GABA is formed, it is used in its regular inhibitory functions, binding to specific receptors on postsynaptic neurons [14]. After the inhibitory effect of GABA has taken place, it is taken back by surrounding glial cells. Once inside these cells, GABA is transformed back to Glutamate by a process called GABA shunt. This process involves a series of enzymatic reactions, leading to the synthesis of glutamate. Glutamate is released into the synapse and is then used for the glutamate-glutamine cycle described earlier. These cycles allow the brain to fine-tune neuronal activity, maintaining a balance between



inhibition and excitation. They are also interconnected, which explains why they were all downregulated in the experiments. The entire cycle can be seen in **Figure 3.5**, where a diagram of the cycle is laid down alongside the ion images obtained by ZnO NP of all three molecules.

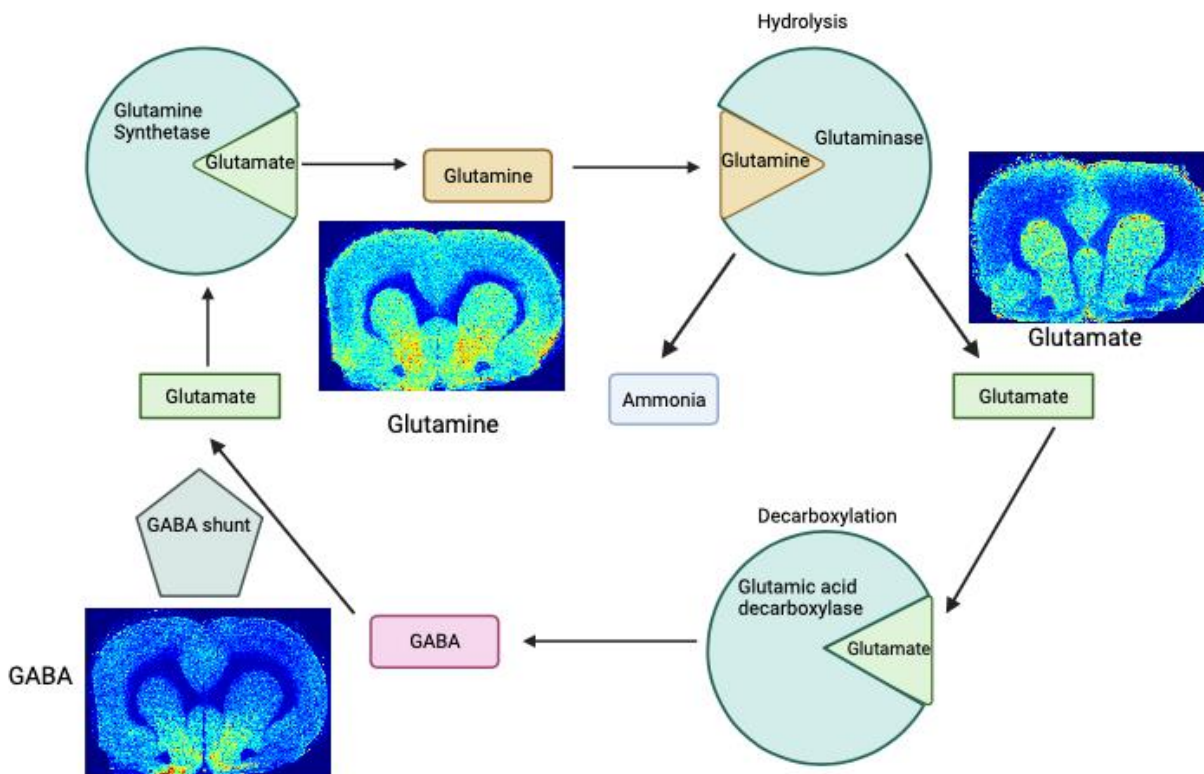


**Figure 3.5.** Diagram of the Glutamate- Glutamine cycle and the GABA- Glutamate cycle. Alongside the diagram, ion images of all three analytes obtained by ZnO NP are shown.

In summary, the MALDI experiments analyzing the effects of chronic adolescent THC edible exposure revealed a consistent decrease in the levels of all three neurotransmitters. Importantly, no significant variations were observed in subregions within the NAc. These changes were statistically highly significant, demonstrating the reliability of ZnO NP as a matrix for the accurate detection of various small molecules.

### 3.3.3 Comparison Between the Relative Quantitation of the Matrices ZnO Nanoparticles and FMP-10 for GABA detection in THC-treated and Vehicle-treated Rat Brains.

Following a similar procedure to ZnO NP, FMP-10 was used to calculate the peak area ratios for GABA. While the spatial distribution using FMP-10 resembled that of ZnO NP, the ion intensities were notably higher in both NAc regions. However, the results obtained through FMP-10 showed notably lower statistical significance in the one-sample t-test for every sex and region, except for NAc shell females where it showed no statistical significance. An interesting difference between the two matrices is that in four distinct THC-treated samples, the GABA ratios appeared unaffected or even elevated. This presents a notable contrast, as all the ratios for ZnO NP were downregulated, as observed in **Figure 3.6**.

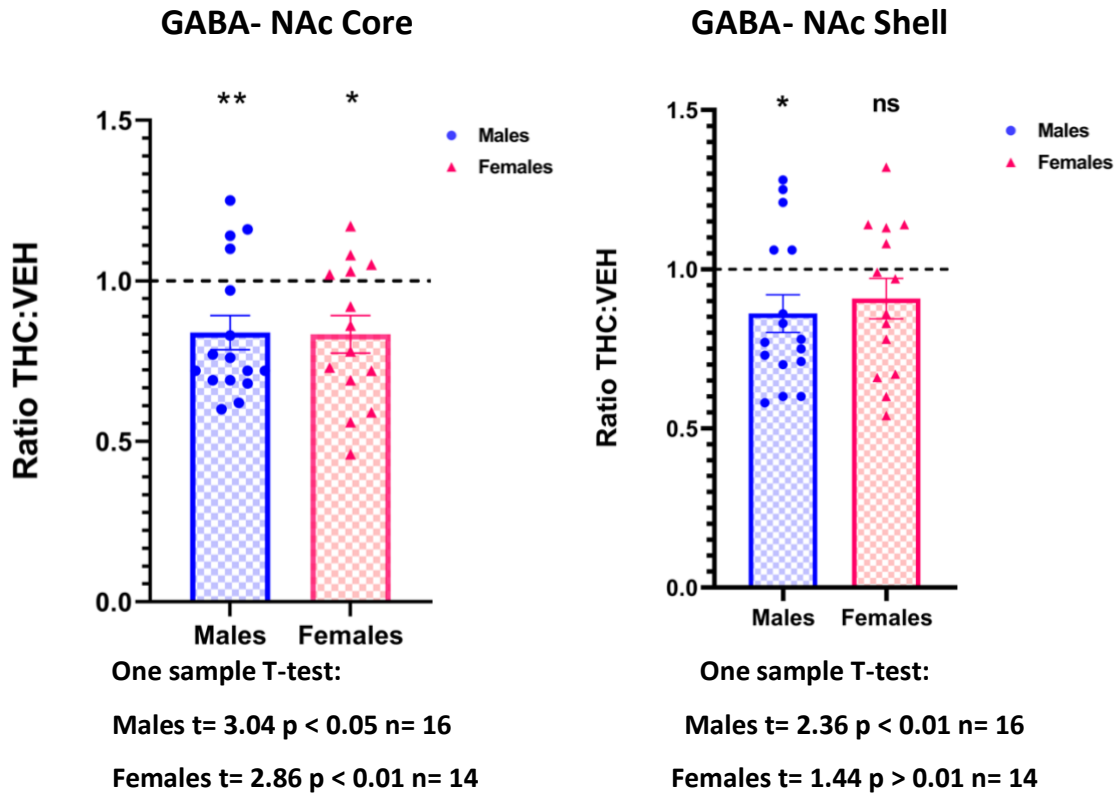


**Figure 3.6.** Peak area ratios of GABA between THC-treated and vehicle-treated adolescent rat brains in the NAc core (left) and shell (right) regions using FMP-10. Asterisks indicate that the featured ratio is statistically significant in the one-sample T-test (\*  $p < 0.01$ )

Currently, definitively determining which matrix is more effective in detecting changes in GABA within biological tissue presents a significant challenge. On one hand, FMP-10 is renowned as a gold standard for detecting neurotransmitters in the field. Its ion intensities across all experiments were impressive, notably surpassing those of ZnO NP. However, despite its impressive ion intensities, the outcomes it produced were less statistically significant than with ZnO NP, although the trend follows the results given by the intensities yielded by the ZnO NP matrix.

Conversely, the ZnO NP matrix consistently yielded highly significant statistical changes in all the regions, albeit with overall lower signal intensities. Both matrices exhibited similar ion distributions, indicating their ability to detect the same molecule.

The current discrepancy in the results obtained by both matrices lacks a clear explanation. However, one potential explanation could lie in how they ionize GABA. For instance, FMP-10's OTCD process might be influenced by external factors such as temperature and reaction duration. In contrast, the ZnO NP matrix avoids the complexities associated with OTCD, but it might have its limitations, such as lower ionization efficiency compared to FMP-10.

It is worth noting that the Laviolette lab has previously conducted similar MALDI MSI experiments that demonstrated statistically significant declines in the NAc region [8]. However, it's important to highlight that these experiments did not involve edibles; instead, THC was introduced directly into the rats' bloodstream.

Ultimately, the establishment of more accurate and robust quantitative methods must be developed to accurately evaluate which matrix is better suited for these investigations. Approaches like normalizing using total ion count (TIC) could be employed before calculating peak area ratios. Moreover, developing calibration curves using standards on tissue might be instrumental in understanding the ionization characteristics for both matrices in a more detailed manner.

### 3.4 Comparison with Literature

The current experiment represents a novel approach in the field of THC research, which consequently leads to a scarcity of directly relevant literature. For example, the administration of THC via the edible route is seldom studied, and its impact on neurotransmitter levels has not been measured to date. As a result, information from existing literature must be extrapolated from studies involving THC injections or electrophysiological data that focus on the activity of neurotransmitters such as Glutamate or GABA. Another constraint is that this experiment examines the effects of chronic THC exposure during adolescence, investigating its lasting impact on adulthood. Such a combination of conditions is not readily found in the existing literature.

Laviolette *et al.* conducted an animal model study that suggested cannabis use during adolescence increases the risk of developing psychiatric disorders in adulthood, including anxiety and depression [2]. The repeated and excessive stimulation of cannabinoid receptors by THC during adolescence seems to disrupt the balance of GABAergic input on pyramidal neurons. This mechanism potentially explains the downregulation of all three target molecules observed in this study. Three years later, Laviolette and Renard published another study examining the impact of adolescent THC exposure on the prefrontal cortex of rats. Using Western blots in the prefrontal cortex, Renard discovered significant increases in trait anxiety levels following adolescent THC exposure, which is consistent with their previous work [15]. Anxiety disorders often involve an imbalance in neurotransmitters, including GABA. As previously explained, when GABA levels are reduced, the brain's ability to regulate stress responses becomes compromised, leading to heightened anxiety levels.

In 2019, a study examined the glutamatergic expression in adolescent male and female rats following the consumption of THC edibles in gelatin form for 15 intermittent access days. Interestingly, the results revealed that female rats exhibited no changes in the NAc core, while male rats showed a downregulation in glutamatergic neurons. In the present MALDI MSI study, a downregulation in glutamate was observed, although it was in both sexes and not just in males like

in the 2019 study [16]. It's noteworthy to highlight that the study didn't track the estrus cycle of the female rats, which could potentially explain the differences observed between sexes.

Several key distinctions between the two studies are worth noting. First, the time frame differs significantly: the 2019 study administered edibles for only 15 days, whereas the current study spanned a longer duration, providing more opportunity for neurotransmitter level changes to occur. Additionally, the concentration of THC in the gelatin edibles used in the 2019 study ranged from 2 to 3 mg/kg, while the current study gradually increased from 1 to 5 mg/kg. These differences in experimental design likely contributed to the conflicting results between the two studies.

Another notable difference between these studies and the current one is the aspect they assessed about neurotransmitters. While the earlier studies examined neurotransmitter expression, encompassing factors like release and synthesis, the current study employed MALDI to measure the overall levels of neurotransmitters present in the targeted regions.

In summary, there is a good agreement between the present study and previous reports found in the literature; any discrepancies found could be explained by the different methods used to administer the THC (injection/ gelatin edible vs. Nutella edible), the duration of THC exposure, and the focus on neurotransmitter level versus neurotransmitter expression.

### 3.5 Conclusion

With the assistance of MALDI MSI, the previously optimized ZnO NP matrix successfully detected and directly visualized the distributions and abundances of glutamate, glutamine, and GABA in the brains of adolescent rats exposed to edible THC. The relative quantitation of the three molecules between THC-treated and vehicle-treated samples was conducted in the NAc core and shell to further investigate each subregion's interaction with THC. A downregulation of GABA, glutamate, and glutamine levels was observed in both the NAc core and NAc shell, underscoring the proficiency of ZnO NP in detecting and analyzing small molecules. Subsequently, a one-sample t-test was applied to the calculated ratios between THC-treated and vehicle-treated samples, confirming that all changes were highly statistically significant ( $p < 0.001$ ).

Additionally, a parallel study employing FMP-10 as the matrix instead of ZnO NP was conducted. While the signals achieved with FMP-10 exhibited considerably higher intensity, the results indicated lower statistically significant differences in most subregions and no statistical significance for female NAc Shell for GABA detection. While a definitive answer on which matrix is better suited for GABA detection remains elusive, this study effectively demonstrates the capacity of MALDI MSI to identify small molecules and elucidate the types of inquiries this methodology can address.

### 3.6 References

- [1] Miech RA, Johnston LD, O'Malley PM, Bachman JG, Schulenberg JE, Patrick ME. *Institute of Social Research* **2020**, Volume I.
- [2] Renard, J., Krebs, M. O., Le Pen, G., & Jay, T. M., *Frontiers in neuroscience* **2014**, 8, 361.
- [3] Stinson, F. S., Ruan, W. J., Pickering, R., & Grant, B. F., *Psychological medicine* **2006**, 36(10), 1447-1460.
- [4] Ferland, J. M. N., Ellis, R. J., Betts, G., Silveira, M. M., de Firmino, J. B., Winstanley, C. A., & Hurd, Y. L., *JAMA Psychiatry* **2023**, 80(1), 66-76.
- [5] Schauer, G. L., King, B. A., Bunnell, R. E., Promoff, G., & McAfee, T. A., *American journal of preventive medicine* **2016**, 50(1), 1-8.
- [6] Reboussin, B. A., Wagoner, K. G., Sutfin, E. L., Suerken, C., Ross, J. C., Egan, K. L., ... & Johnson, R. M., *Drug, and alcohol dependence* **2019**, 205, 107660.
- [7] Sarikahya, M. H., Cousineau, S., De Felice, M., Lee, K., Wong, K. K., DeVuono, M. V., ... & Laviolette, S. R., *Eneuro* **2022**, 9(5).
- [8] De Felice, M., Chen, C., Rodríguez-Ruiz, M., Szkudlarek, H. J., Lam, M., Sert, S., ... & Laviolette, S. R., *Neuropsychopharmacology*, **2023**, 48(3), 540-551.
- [9] Banich, M. T.; Floresco, S. *Cognitive Affective & Behavioral Neuroscience* **2019**, 19, 409-414.
- [10] McKenna, M. C., *Journal of Neuroscience Research*, **2007**, 85(15), 3347-3358.
- [11] Cohen, K.; Weizman, A.; Weinstein, A. *European Journal of Neuroscience* **2019**, 50, 2322-2345.
- [12] Butt, A. M.; Fern, R. F.; Matute, C. *Glia* **2014**, 62(11), 1762-1779.
- [13] Bak, L. K., Schousboe, A., & Waagepetersen, H. *Journal of neurochemistry*. **2006**, 98(3), 641-653
- [14] Walls, A. B., Waagepetersen, H. S., Bak, L. K., Schousboe, A., & Sonnewald, U. *Neurochemical research*. **2015**, 40, 402-409
- [15] Renard, J., Rosen, L. G., Loureiro, M., De Oliveira, C., Schmid, S., Rushlow, W. J., & Laviolette, S. R., *Journal of Neuroscience* **2016**, 35(18), 5160-5169
- [16] Kruse, L. C., Cao, J. K., Viray, K., Stella, N., & Clark, J. J., *Neuropsychopharmacology* **2019**, 44(8), 1406-1414



## **Chapter 4. Conclusions and Future Work**

## 4.1 Conclusions and Future Work

Mass spectrometry imaging (MSI) is an exceptional technique for detecting and visualizing the spatial distributions of small molecules in biological tissue sections. Unlike other methods in the field, it does not require molecular labeling and can rapidly detect a wide range of compounds. Matrix-assisted laser desorption ionization (MALDI) is the optimal ionization technique for MSI, providing excellent spatial distribution while maintaining tissue integrity. Moreover, MALDI is highly versatile, as various matrices enable the detection of diverse analytes including fatty acids, lipids, proteins, and small molecules.

As such, the development of new matrices plays a pivotal role in advancing MALDI as a leading technique in the field. This offers opportunities to detect and image novel analytes with enhanced selectivity and sensitivity. Small molecules present challenges due to their low mass range, often leading to interference with matrix background peaks, hindering their detection. Nanometric materials like metal oxide nanoparticles circumvent these issues by lacking such background signals and possessing desirable matrix characteristics including a relatively high surface area, UV absorbance, and effective heat conductivity. Notably, ZnO nanoparticles (ZnO NP) have demonstrated their suitability for small molecule detection, provided the correct workflow is applied.

With the procedure developed in this work, commercially available ZnO NP exhibited the capability to detect a range of small molecules, including GABA, glutamate, glutamine, and cholesterol, with good spatial resolution and reproducibility. The optimized matrix was showcased in a comprehensive study involving the detection and relative quantification of GABA, glutamate, and glutamine in the brains of adolescent rats exposed to THC edibles. While these results were largely promising in the NAc region and consistent with existing literature, GABA quantification presented differences when compared to another matrix, FMP-10. These discrepancies raise questions about quantification accuracy and ionization efficiency. Nevertheless, the reliability and

reproducibility of ZnO NP as a matrix for small molecule detection are evident, making it a promising choice for future long-term studies.

The potential of ZnO NP is vast and exciting. Certain key neurotransmitters such as dopamine and serotonin cannot be currently detected with the optimized ZnO NP, and the reasons for this remain unclear. Possible explanations include ion suppression in brain tissue, their relatively lower abundance compared to other molecules, and the inherent ionization mechanism of ZnO NP.

Consequently, an important next step could involve enhancing the sensitivity and selectivity of the already optimized ZnO NP matrix through the creation of a hybrid matrix. For example, iron oxide magnetic nanoparticles functionalized with SiO<sub>2</sub> and 2,5-dihydrobenzoic acid (DHB) have been used to control ionization efficiency and interference background [1]. Although these functionalized nanoparticles displayed heightened signal intensity, their use was not explored in imaging experiments or biological samples such as organic tissue. Similarly, TiO<sub>2</sub> NP were functionalized with dopamine, resulting in increased UV light absorption and higher surface pH, enabling the detection of diverse phospholipid signals [2]. This modification enhanced sensitivity and selectivity for Lewis basic compounds like fatty acids and cholesterol in positive mode in rat brain tissue.

A parallel approach could be undertaken for ZnO NP, involving functionalization with an organic molecule like DHB to improve selectivity for hard-to-ionize neurotransmitters. However, achieving the right balance between DHB and ZnO NP material ratios could prove challenging, given that DHB itself can contribute to matrix noise.

Quantitation is another aspect that holds potential for further optimization. Currently, relative quantitation of neurotransmitters between drug-treated and vehicle-treated samples is performed by randomly pairing a single sample from each group onto the same steel plate, followed by matrix

deposition and subsequent imaging. While this approach theoretically minimizes variables like sample preparation and MALDI measurements, it doesn't align well with more extensive studies involving multiple samples per plate. Larger-scale studies, such as incorporating 10 samples per plate, encounter issues due to known errors in the imaging software arising from extended imaging durations exceeding 10 hours.

Normalizing to an internal standard could rectify signal discrepancies arising from sample preparation in biological tissue. In this context, the ion signal intensity of the target analyte from the acquired MSI data would be divided by the corresponding intensity of the internal standard. Ideally, this internal standard should be chemically identical to the target analyte and applied via automated spraying. This approach would minimize both signal fluctuations' variability and any biological variability inherent in these types of studies.

Similar normalization methods could be applied to standards to gain a more comprehensive understanding of the ionization mechanism found in ZnO NP. Establishing a series of diluted GABA standards and subjecting each individually to MALDI analysis to generate a calibration curve would provide a deeper insight into the way ZnO NP functions as a matrix. Furthermore, varying conditions beyond standard concentrations could be explored. For instance, employing mixtures of analytes (such as GABA, glutamate, and fatty acids) to investigate potential ion suppression effects or any ionization preferences.

Understanding the matrix's ionization mechanism could shed light on the diverging results yielded by FMP-10 and ZnO NP in the adolescent edible THC study. This approach has the potential to help us better understand the complexities of the technique and uncover the key factors that are responsible for the observed differences.

## 4.2 References

- [1] Tseng, M. C., Obena, R., Lu, Y. W., Lin, P. C., Lin, P. Y., Yen, Y. S., ... & Chen, Y. J., *Journal of the American Society for Mass Spectrometry* **2010**, 21. 1930-1939.
- [2] Wu, Q., Chu, J. L., Rubakhin, S. S., Gillette, M. U., & Sweedler, J. V., *Chemical science* **2017**, 8(5), 3926-3938.

# Curriculum Vitae

## Education

**Western University, London, Canada**

09/2021- present

Department of Chemistry

Candidate of M. Sc.

Supervisor: Dr. Ken Yeung

**Universidad de las Américas Puebla, Cholula, Mexico**

08/2017- 05/2021

Major: Nanotechnology and Molecular Engineering

Degree: Bachelor of Science

## Research Experience

**Western University, London, Canada**

09/2021- 05/2023

- Developed methods for Matrix-assisted Laser/ Desorption Ionization Mass Spectrometry Imaging (MALDI MSI) for the detection of small molecules in rodent brain tissue.
- Optimized commercially available ZnO NP as a matrix and ensured its compatibility with automatic sprayers for its deposition.
- Participated in a variety of collaborations with the Neuroscience Department at Western University applying the developed MALDI MSI protocols in biological studies.

**Universidad de las Américas Puebla, Cholula, Mexico**

08/2017- 05/2021

- Synthesized TiO<sub>2</sub> nanofibers via electrospinning and Graphene Oxide via Hummers method for the treatment of wastewater contaminated with Dyes

## Work Experience

**Graduate Teaching Assistant**

09/2021- 05/2023

**Department of Chemistry, University of Western Ontario, London, Canada**

Organic Chemistry for Life Sciences and Organic Chemistry of Biological Molecules

- Conducted pre-laboratory talks on different laboratory techniques and theories

- Assisted in laboratory activities, including setting up equipment and guiding students during lab sessions
- Graded assignments and quizzes, ensuring adherence to the grading guidelines for fairness and consistency

**Chair of International Graduate Student Issues Committee (IGSIC)** 10/2021- 06/2023

### **University of Western Ontario, London, Canada**

- Fostered an inclusive and welcoming environment for graduated students from diverse backgrounds at Western University.
- Engaged in active advocacy for equitable practices, striving to eliminate biases and barriers in the graduate student environment.
- Organized graduate student events to encourage a more inclusive graduate culture at Western University.

## **Publications**

Jimenez-Cisneros, J., Galindo-Lazo, J. P., Mendez-Rojas, M. A., Campos-Delgado, J. R., & Cerro-Lopez, M. (2021). Plasmonic spherical nanoparticles coupled with Titania nanotube arrays prepared by anodization as substrates for surface-enhanced Raman spectroscopy applications: a review. *Molecules*, 26(24), 7443.

## **Presentations**

**Mass Spectrometry Imaging of Small Molecules in Rodent Brain Tissue.** Samantha Cousineau, **Juan Pablo Galindo Lazo**, Mathusha Pusparajah, Steven R. Laviolette, Ken K.-C. Yeung. Western Institute for Neuroscience Reception (London, CA, May 2023). Poster

**Administration of N-Acetylcysteine Prevents the Long-lasting Depressive-like Phenotypes Induced by Adolescent THC Exposure.** Marta De Felice, Hanna J. Szkudlarek, Mar Rodríguez-Ruiz, Taygun C. Uzuneser, Mohammed H. Sarikahya, Mathusha Pusparajah, **Juan Pablo Galindo Lazo**, Shawn N. Whitehead, Ken K.-C. Yeung, Walter J. Rushlow, Steven R. Laviolette. International Cannabinoid Research Society Symposium (Toronto CA, June 2023). Poster and Presentation.

**MALDI MS Imaging of Small Molecules in Rat Brain Tissue with Zinc Oxide Nanoparticles (ZnO NP) and Removal of NP Aggregates by Filtration.** **Juan Pablo Galindo**, Natalie Merola, Kristina Jurcic, Steven R. Laviolette, Ken K.-C. Yeung. Annual American Society for Mass Spectrometry Conference (Houston, USA, June 2023). Poster

**Neuronal and molecular maladaptation produced by adolescent edible delta-9-tetrahydrocannabinol (THC) consumption.** DeVuono, M. V., Anderson, S., Pusparajah, M., **Galindo Lazo, J.P.**, Sarikahya, M. H., Szudlarek, H. J., De Felice, M., Yeung, K.K. -C., Laviolette, S. R. Society for Neuroscience 2023 (Washington, USA, November 2023). Poster

## **Course Work**

9621 Bioinorganic Chemical Methods 88

9522 Analytical Separations 86